In-situ Internal Study of Liquid Binder Penetration and Nucleation Dynamics in Wet Granulation of Pharmaceutical Powders using Synchrotron X-ray Imaging

A Thesis Submitted to the College of Graduate and Postdoctoral Studies

in partial fulfillment of the requirements for the degree of

Master of Science

in the Department of Chemical and Biological Engineering

University of Saskatchewan

Saskatoon

By

Sima Zeinali Danalou

Permission to Use

The author has agreed that the Libraries of the University of Saskatchewan may make this thesis freely available for inspection. Moreover, the author has agreed that permission for extensive copying of this thesis for scholarly purposes may be granted by the professor(s) who supervised the thesis work recorded herein or, in their absence, by the Head of the Department of Chemical and Biological Engineering or the Dean of the College of Graduate and Postdoctoral Studies. Copying or publication or any other use of the thesis or parts thereof for financial gain without written approval by the University of Saskatchewan is prohibited. It is also understood that due recognition will be given to the author of this thesis and to the University of Saskatchewan for any use of the material of the thesis.

Requests for permission to copy or to make other use of the material in this thesis in whole or in part should be addressed to:

Head of the Department of Chemical and Biological Engineering

University of Saskatchewan

57 Campus Drive

Saskatoon, Saskatchewan

S7N 5A9

Canada

OR

Dean

College of Graduate and Postdoctoral Studies

University of Saskatchewan

116 Thorvaldson Building, 110 Science Place

Saskatoon, Saskatchewan S7N 5C9 Canada

Abstract

Wet granulation is a common form of granulation with a liquid binder, having broad applications in the chemical and pharmaceutical industries. In order to produce high-quality granules, it is essential to continuously monitor the granule's microstructure during the granulation process. Wet granulation is a fast process and pharmaceutical powders are typically opaque in nature. So conventional methods cannot capture wet granulation internally. In contrast, synchrotron X-ray imaging techniques allow for visualization of the internal fast process due to higher photon flux, compared to lab-based X-ray imaging.

This study employed the synchrotron X-ray imaging technique to examine the internal characteristics of powder beds and how they influence the dynamics of single droplet penetration and the microstructure of the dry granule. The single-drop impact method was used to obtain in-depth knowledge of the process of wet granulation. In this study, the liquid binders were deionized water and isopropanol, and the powders were binary mixtures of acetaminophen (APAP) as the active pharmaceutical component, with lactose monohydrate (LMH) and microcrystalline cellulose (MCC), two common excipients.

An internal analysis of powders revealed that, for particles of various sizes, increasing the excipient led to the presence of more void spaces and thereby increased the porosity. It is essential to understand the powder's mixing quality before granulation. A higher mixing quality was obtained by increasing the APAP component. In general, MCC mixtures exhibited fewer aggregations and more uniform pore distribution than those from LMH ones. The spreading and vertical imbibition of an isopropanol droplet during penetration exhibited competing behaviors, demonstrating that penetration in coarse MCC powders followed a more linear vertical movement, mostly because of aligned pore distribution. For the first time, the internal rapid nucleation

with liquid binders was studied. Granules in more uniformly distributed, coarser, and homogeneous powders experienced a faster rate of pore evolution during the nucleation. Wetting investigations revealed that the non-uniform pore distribution in powder beds was responsible for the Crater mechanism for the majority of the 50% of excipients. For MCC with the largest droplet diameter growth, the Spreading mechanism was observed, and for 90% of fine LMH with the longest penetration length, the Tunneling occurred. The spreading and Tunneling mechanisms produced final granules with the highest and lowest porosity, respectively.

In-situ monitoring of the wet granulation process using synchrotron X-ray imaging was demonstrated in this work, and for the first time, data on pore studies throughout the nucleation and growth stages were provided. This study revealed how wet granulation and the resulting granules were affected by liquid-powder interactions. The new information gained from this research will be highly helpful for choosing the desirable powders and process conditions for granulation processes in the chemical and pharmaceutical industries.

Acknowledgments

Table of Contents

vi

List of Figures

x

List of Tables

Nomenclature

Notation	Description
AR	Aspect Ratio
Bo_g^*	modified Bond number
CDA	constant drawing area
D_a	projected area equivalent diameter (mm)
D_{max}	final granule maximum diameter, (mm)
D_{min}	final granule minimum diameter, (mm)
D_M	maximum spreading width, (mm)
D_0	initial droplet width, mm
$\bar{D}$	dimensionless diameter
d_s	surface mean diameter, (µm)
d_{50}	median particle size, (µm)
g	gravitational acceleration constant, 9.8 m/s^2
H_g	final granule height, (mm)
HAR	D_{max}/D_{min}
H_0	initial droplet height, mm
$\bar{H}$	dimensionless height
MI	mixing index
L	penetration length, (mm)
R_{imb}	imbibition rate, s^{-1}

RSD	relative standard deviation
r_d	droplet radius, (mm)
t^*	final penetration time, (s)
$\bar{t}$	dimensionless time
VAR	D_a/H_g
V_0	initial droplet volume, (μL^3)
V(t)	droplet volume remaining at the bed surface, $(\mu L\ )$

Greek letters

γ	liquid surface tension (mN/m)
θ_0	initial contact angle (°)
θ_M	maximum contact angle, (°)
$\bar{\theta}$	dimensionless contact angle
ρ_p	particle skeletal density, (g/cm^3)
ρ_{bed}	particle bulk density, (g/cm^3)
σ	standard deviation
σ_0^2	variance of desired material at complete segregation
σ^2	variance of desired material at actual mixing condition
σ_r^2	variance of desired material at complete mixing

Abbreviations

Abbreviation	Meaning
APAP	acetaminophen
API	active component
BMIT	Biomedical Imaging and Therapy Facility
CLS	Canadian Light Source
CT	Computed tomography
FOV	field of view
LMH	lactose monohydrate
LMHF	lactose monohydrate fine
MCC	microcrystalline cellulose
MCCF	microcrystalline cellulose fine

Chapter 1. Introduction

1.1 Organization of the Thesis

The thesis is written in a manuscript-based style with five chapters. Chapter 1, is the thesis introduction which includes the project motivation, knowledge gaps, objectives, hypothesis, and thesis organization. A literature review of current studies on the wet granulation process and mechanisms, mixing and segregation, final granules characterizations, and visualization techniques are presented in Chapter 2. Chapter 3 contains the first manuscript which analyzed the static powder pore studies and penetration dynamics. Chapter 4 is based on the second manuscript with a focus on analyzing the nucleation dynamics and final granule microstructure, further revealing the novelty of this study. Chapter 5 covers the main conclusions drawn from this project and recommendations are also provided for future research. The references are given at the end of each associated chapter.

1.2 Project Motivation and Knowledge Gap

Granulation is one of the important unit operations in the chemical and pharmaceutical industries, enabling better control of the drug concentration, especially at a lower fraction. Wet granulation is the most popular granulation method predominantly used in the pharmaceutical industry [1]. Wet granulation is the agglomeration of finer particles in the presence of a liquid binder to produce larger structures [2]. Figure 1.1 shows the schematic of stages in conventional wet granulation processes. As can be seen, prior to wet granulation, the mixing quality and segregation status of the powder blend is critical to ensure that the fraction of APIs will be the same in all downstream tablets [3]. Moreover, the porosity and pore size of the powders is another predominant factor influencing the liquid flow and wet granulation process, and the properties of the final tablets [4, 5]. Finally, it is crucial to produce granules/tablets with desirable specifications. Granule size

distribution, density, hardness, tensile strength, disintegration, and dissolution behavior are some of the most important attributes of tablet formulation. For example, if the granules are extremely hard, this may compromise the drug release profile [1]. Consequently, the microstructure study of the tablets could reveal the correlation between micro-scale and aforementioned macro-scale properties.
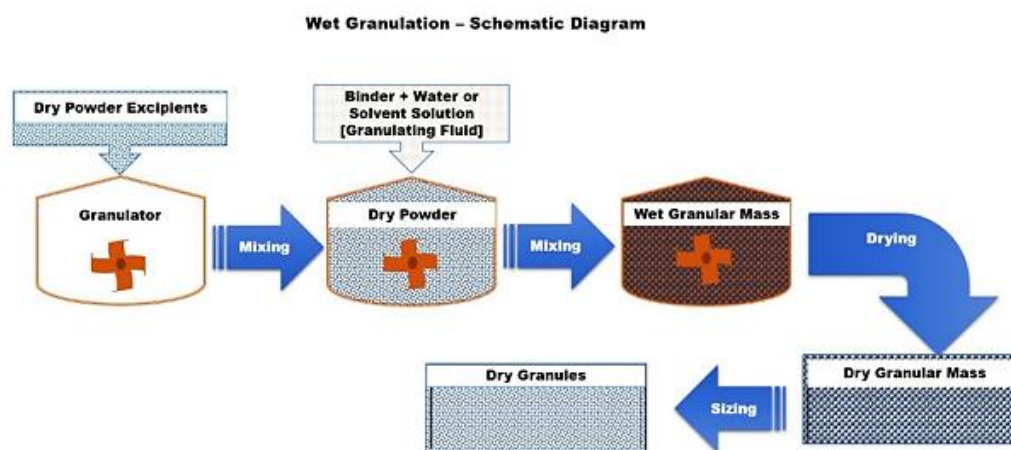
Figure 1. 1. Schematic diagram of melt granulation [6]

Three main stages take place during the wet granulation process, including wetting and nucleation (the fastest step taking place in milliseconds or seconds), consolidation and growth, and breakage and attrition [6]. These rate processes are dependent on both external process factors, namely granulator and operating conditions, and formulation, namely the type of binders and powders [7].

Recently, an internal study of a process has increasingly received research attention, as it gives vital information to understand the process, end product properties, and scaling up. Most studies on internal structure have been conducted on the final granules. And, due to the opaque nature of pharmaceutical powders and the fast and complex liquid-solid interactions, lab-based methods fail to capture the wet granulation process internally. Synchrotron X-ray

imaging techniques are one of the most emerging techniques, and receive more significant interest than conventional X-ray imaging techniques due to the following reasons [8]:

1. The very high flux density of synchrotron X-ray reduces the exposure time resulting in the signal-to-noise ratio improvement and enabling fast radiographic imaging.

2. Wavelength tunability allows using the optical wavelength to investigate objects with different absorption coefficients.

3. The coherence of the beam has the advantage to image low-density objects with a low absorption coefficient and producing high contrast images.

As a result, synchrotron X-ray imaging becomes one of the minimally invasive imaging techniques due to its fast imaging and monochromatic beam and reducing the low energy un-wanted beams scatterings.

1.3 Objectives

The objectives of this project were to employ synchrotron X-ray imaging techniques to:

1. Assess mixing quality, porosity measurement, and particles and pores distribution of static powder beds made of binary mixtures containing both APIs and excipients;

2. Study penetration dynamics, porosity, and pore evolution measurement over time, and to determine granulation mechanisms; and.

3. Investigate morphology and microstructures of the final granules.

1.4 Hypothesis

Synchrotron X-ray imaging techniques can capture and visualize the internal dynamic wet granulation, because of its high temporal and spatial resolution.

1.5 References

[1]   P. Thapa, D. H. Choi, M. S. Kim, S. H. Jeong, "Effects of granulation process variables on the physical properties of dosage forms by combination of experimental design and

principal component analysis", *Asian J. Pharm. Sci.*, vol. 14, no. 3, pp. 287–304, 2019, doi: 10.1016/j.ajps.2018.08.006.

[2] S. M. Iveson, J. D. Litster, "Fundamental studies of granule consolidation. Part 2: Quantifying the effects of particle and binder properties", *Powder Technol.*, vol. 99, no. 3, pp. 243–250, 1998, doi: 10.1016/S0032-5910(98)00116-8.

[3] S. Oka *et al.*, "The effects of improper mixing and preferential wetting of active and excipient ingredients on content uniformity in high shear wet granulation", *Powder Technol.*, vol. 278, pp. 266–277, 2015, doi: 10.1016/j.powtec.2015.03.018.

[4] R. P. Dias, J. A. Teixeira, M. G. Mota, A. I. Yelshin, "Particulate binary mixtures: Dependence of packing porosity on particle size ratio", *Ind. Eng. Chem. Res.*, vol. 43, no. 24, pp. 7912–7919, 2004, doi: 10.1021/ie040048b.

[5] X. He, X. Han, N. Ladyzhynsky, R. Deanne, "Assessing powder segregation potential by near infrared (NIR) spectroscopy and correlating segregation tendency to tabletting performance", *Powder Technol.*, vol. 236, pp. 85–99, 2013, doi: 10.1016/j.powtec.2012.05.021.

[6] D. M. Parikh (Ed.), Handbook of pharmaceutical granulation technology. Taylor & Francis Group, 2005.

[7] P. Suresh, I. Sreedhar, R. Vaidhiswaran, A. Venugopal, "A comprehensive review on process and engineering aspects of pharmaceutical wet granulation", *Chem. Eng. J.*, vol. 328, pp. 785–815, 2017, doi: 10.1016/j.cej.2017.07.091.

[8] C. Karunakaran *et al.*, "Factors influencing real time internal structural visualization and dynamic process monitoring in plants using synchrotron-based phase contrast X-ray imaging", *Sci. Rep.*, vol. 5, no. 1, p. 12119, 2015, doi: 10.1038/srep12119.

Chapter 2. Literature Review

2.1 Pharmaceutical Tablets Formulation

In the pharmaceutical industry, tablets generally contain excipients and an Active Pharmaceutical Ingredient (API). Excipients can be characterized into two categories, including bulk agents or fillers, in the case that the drug dose is low, and functional additives (binders, disintegrants, lubricants, colorants, and stabilizing agents). The kind of excipients required depends on the type of drug, process, formulator, and cost of material [1].

Lactose, dicalcium phosphate, microcrystalline cellulose (MCC), starch, and pregelatinized starch are used as fillers [2]. Fillers help tablets to have desired size and weight [1]. The typical liquid binders used in the pharmaceutical industry are water, ethanol, and isopropanol [1]. They are employed to adhere to the particles. Generally, the viscosity of the binder plays an important role in the rate of granule size enlargement [2]; for instance, if the binder viscosity was low, the granules would be too large with insufficient strength [3], or granules typically experience lower consolidation and higher porosity when the surface tension of the binder is reduced [4].

Starch, cellulose, cross-linked polyvinylpyrrolidone, sodium starch glycolate, and sodium carboxymethylcellulose are commonly used as disintegrants. A disintegrant helps tablets split into small fragments while they contact liquid and increase the drug release rate [1]. Tablets typically have lubricants to reduce attrition between pharmaceutical powders and metal surfaces of processing equipment. For the identity and appropriate appearance of tablets, colors are used [1]. Also, a stabilizing agent such as a surface-active agent is needed to help APIs to maintain the desirable properties of the product [1].

2.2 Wet Granulation

Granulation is one of the most important unit operations in chemical engineering industries (e.g., pharmaceutical, detergent production, and fertilizer). Granulation is known as the agglomeration process where particles combine to make larger agglomerates. Granulation results in improvements, including, hardness, dustiness hazard reduction, caking and segregation prevention, bulk density, and powder handling [5, 6]. Granulation is very important in the pharmaceutical industry, as it provides the control of drug homogeneity at low concentrations of drug and specified product bulk density [7]. Granules themselves could be utilized as a pharmaceutical dosage, but they are more commonly used as an intermediate product in tablet manufacturing [8]. Granulation processes can be divided into two main groups: dry granulation and wet granulation, depending on whether a liquid binder is utilized in manufacturing. Dry granulation includes direct compression, slugging, and roller compactor. And it is employed when the material in the process may be sensitive to moisture and heat [2]. However, wet granulation has been shown to have low operation cost, better control of active component fractions at low dose fractions, higher product bulk density, and better compatibility [9]. At least one wet granulation step was employed in 46.7% of the tablets and 18.6% of the capsule manufacturing process [8]. Wet granulation is commonly performed in high shear granulators, twin screw granulators, and fluidized beds, where granulation takes place by impellers, screws, and fluidizing air, respectively [7].

2.2.1 Granulation Process in a Single Drop Impact Method

Several works used the single droplet method to investigate wet granulation and to study the effects of powder packing on granule formation and final granule homogeneity properties [10–14].

In a wet granulation process, granules are formed in three steps: wetting and nucleation, granule growth and consolidation, and breakage and attrition [15]. Figure 2.1 illustrates the granulation steps. The nucleation is the first immediate coalescence after a drop contacting with dry powders; the bonds between particles form once the liquid is distributed. The nucleation of the particles is substantially affected by the wetting step. Wetting and nucleation steps are affected by a few factors such as liquid binder viscosity, density, wettability, and liquid droplet size. For example, surfactants and other wetting agents are widely used to improve poorly wetting materials [7]. The collision between original wetted particles leads to growth. The binding of particles occurs when the capillary pressure, surface tension, and viscous forces are applied. The capillary pressure drives liquid flow, while is opposed by viscous losses and the pressure of air trapped inside the pores [16]. The consolidation stage directly influences voidage of the granules and, subsequently, the strength, hardness, and dissolution characteristics of the resultant granules. If the wet or dried granules are internally weak, they will be easily affected by attrition due to compaction in granulators or subsequent powder handling processes [15].
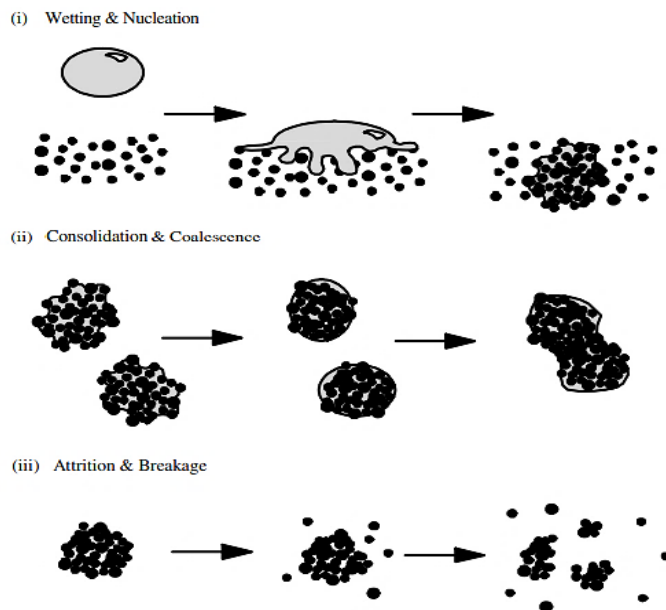
Figure 2. 1. Schematic of granulation processes [13].

.

Figure 2.2 shows typical wet granulation steps along with their influencing parameters.
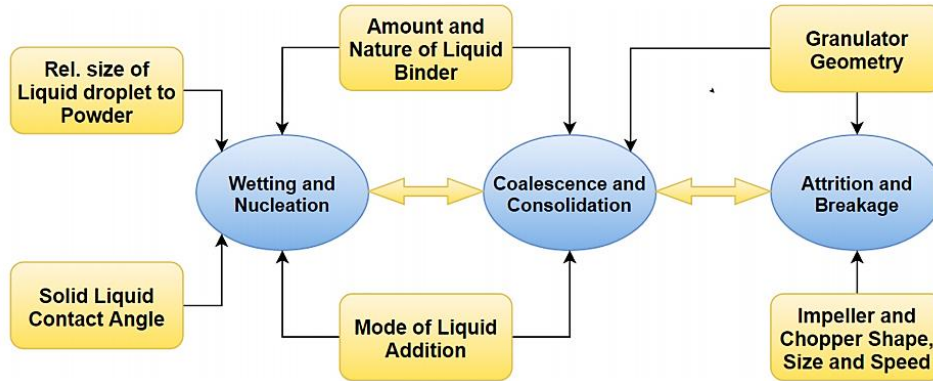
Figure 2. 2. Steps in wet granulation with operating parameters [8].

2.2.2. Granulation Mechanisms in Single Drop Impact Method

In the wetting stage of the wet granulation process, a combination of spreading and imbibition occurs as the droplet penetrates the powder bed [17]. Three probable granulation mechanisms occur when a single drop contacts a powder bed: Tunneling, Spreading, and Crater Formation [13]. Granules are generated in more cohesive powder beds via Tunneling formation, where particles aggregate around droplets and subsequently tunnel into powders. At low binder droplet impact velocities and larger particles, the Spreading mechanism occurs. If the droplet has a high impact velocity, a crater would be formed in the powder bed, resulting in the Crater mechanism [10]. Figure 2.3 is the schematic of three granule formation mechanisms.

Emady et al. [10] presented that dimensional analysis (an increase in the crater size) and a range of modified Bond numbers (Bo_g^*) (ratio of the capillary force to the gravitational force) are two ways to specify the granule formation mechanism. The modified Bond number is determined by liquid surface tension, the powder-liquid contact angle, the surface mean particle diameter and particle bulk density. The Spreading and Crater formation occur when Bo_g^*<65,000, and the

Tunneling happens when $Bo_g^* > 65,000$. Also, Gao et al. [11] studied hydrophobicity and primary particle size influence on the mechanisms. They argued that despite hydrophobicity, the particle size has a greater impact on the granule formation, granule internal structure, and content homogeneity. Moreover, there are correlations between powder packing and granulation process, and product properties. Bed porosity and pore structure are important factors affecting permeability and fluid flow or liquid mass transfer within the porous media [18]. Porosity is dependent on particle size, particle size distribution, and particle shape under specified packing circumstances. Due to the fact that industrial powders often deviate from ideal assumptions of spherical, smooth, and solid particles, the numerical models typically fail to provide a reliable estimate [19].
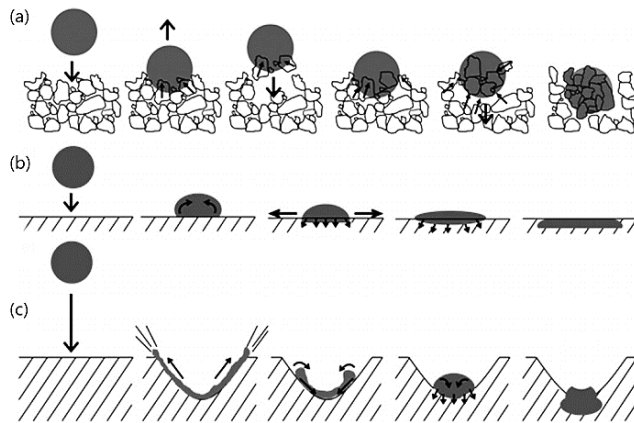
Figure 2. 3. Three granule formation mechanisms: (a) Tunneling, (b) Spreading, and (c) Crater [17].

2.3 Qualifications of Pharmaceutical Powder Beds

2.3.1 Mixing and Segregation

Mixing and segregation are essential in industries dealing with granular materials (e.g., pharmaceuticals, chemicals, agriculture, catalysts, and foods). Segregation is referred to the separation of one component in a mixture from the other component(s) [19]. Within granulation processes, one of the key product qualities in the pharmaceutical industry is the homogeneity of

9

ingredients, especially in low-dose granules. The desired proportion of APIs and the excipients in the final granules must be the same as the bulk mixture [20]. Otherwise, there could be a failure in drug release and pharmaceutical preparation dissolution characteristics [21].

Based on the criteria considered, segregation could be classified differently. The most common approach for classification is the segregation mechanism. The four proposed patterns would be trajectory, sieving (percolation), elutriation (fluidization), and agglomeration segregation. In the pharmaceutical industry, sieving, elutriation, and agglomeration occur prevalently [22]. Also, interparticle forces (e.g., van der Waals and surface tension) in agglomeration segregation lead to the formation of agglomerates. Figure 2.4 shows the aforementioned four patterns.
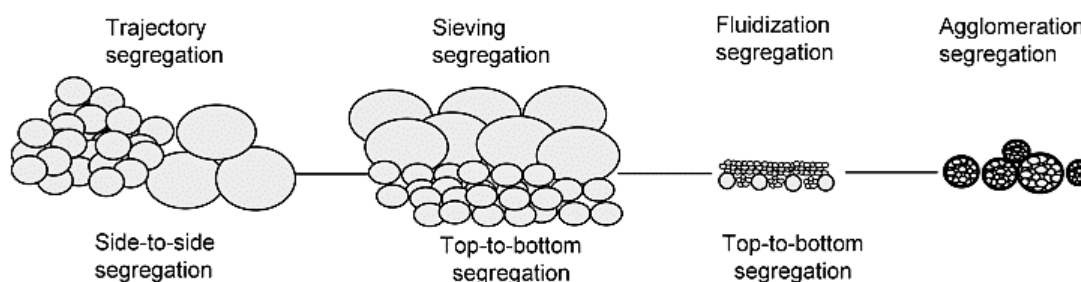
Figure 2. 4. Schematic of four segregation patterns [25].

The factors affecting segregation could be classified as follows: material properties, device and operation parameters, handling methods, and environmental conditions. The most influential material properties for segregation include size ratio (or size distribution), absolute or mean particle size, particle concentration, particle shape, and density [22]. However, regardless of other factors, cohesive powders are less likely to be segregated [23]. The main cause of powder segregation is particle size differences [2]. It has been proved that segregation is more probable for a wide-size distribution [19]. Dries et al. [24] concluded that finer particles were accumulated around coarse granules. And generally, for segregation, a minimum size ratio of 2:1 to 3:1

is required [22]. Generally, by keeping a relatively significant mass fraction of the fine constituent, the degree of segregation could be minimized [25]. Also, segregation is much higher when a binary mixture consists of irregular shapes (e.g., angular), coarse particles, and spherical-shaped fine particles. He et.al, [26] discussed that the more similar the Aspect Ratio (AR) (the ratio of maximum width to minimum width) between the components, the better mixing occurs. For example, the binary mixture of components with AR of 1 and 2 has a higher mixing index than components with AR of 0.5 and 2 [26]. However, compared with the size ratio effect, the effect of the particle shape on segregation is not significant.

In order to minimize particle segregation, several approaches are used. The most effective way is to reduce the particle size distribution. Furthermore, by decreasing the particle size, segregation can be minimized [22]. Increasing the cohesiveness of materials by adding water or oil could also decrease particle segregation [27]. Moreover, mixing quality is an important factor in the segregation tendency. There are three mixing mechanisms, including diffusive, shear, and convective; the latter is the most likely one to reduce segregation during mixing [28]. Overall, in the case of segregating materials, submerged-impeller mixers are more efficient than tumbler mixers. For example, to break up the agglomerates during mixing, shear forces could be applied through a high-speed impeller [22]. Oka et al. [20] pointed out that by increasing the impeller speed, the demixing extent of the powder mixture (APAP and MCC) would be reduced.

2.4. Final Granules Characterizations

Granules should have proper tensile strength and dissolution behavior, as the two main characteristics. The dissolution rate determines the release rate of the API present in the tablet and it is greatly dependent on the tablet's porosity [29]. Tensile strength, a measure of tablet bond strength, indicates the tablet's ability to avoid deformation during manufacturing, transportation,

and handling. Besides, the tensile strength of a tablet is critical for drug release from formulations [30]. The microstructure of a tablet is greatly related to important pharmaceutical properties such as disintegration, drug release, and mechanical strength, as tablets with similar bulk properties, would have different dissolution behavior due to different microstructures. Tablet porosity is a straightforward way to evaluate the tablet microstructure [31]. Moreover, pore size, shape, and tortuosity are all parameters influencing the tablet microstructure [32].

2.5. Visualization and Characterization Techniques

The visualization of dynamic wet granulation is helpful to understand the granulation mechanism and the downstream products. Various techniques have been used and they can be categorized into three non-invasive methods to visualize mixing, segregation, granules processes, and structures: velocimetric, spectroscopic, and tomographic techniques [33].

The optical imaging technique is one of the velocimetric techniques. The first noninvasive techniques relied on cameras to capture videos and photographic phenomena. Kingston et al. [34] compiled optical visualization and composition analysis to assess the mixing quality, through 360° video viewing using four Panasonic HC-V700M HD video cameras, the optical visualization provided a qualitative mixing assessment of the entire mixing region. However, the most significant drawback of digital imaging systems is that only surface phenomena can be explored. When there is a small difference in physical properties (e.g., size) of constitutes, spectroscopic techniques can be used and they focus on the chemical compositions of the sample. For instance, Raman spectroscopy is used for component identification. Imoto et al. [35] used Raman analysis to assess granule morphology in the development of low-content formulations. Using this method, they could study the distribution of the ingredients on the surface of the granules. While the primary drawback of spectroscopic methods is their limited size of inspection in comparison to the entire

sample of the investigated material. Tomographic techniques such as X-ray computed tomography and magnetic resonance imaging, can be used to show the spatial distribution of particles and determine inhomogeneities, while their large power requirements and equipment cost are hindering factors for designing for full-scale industrial systems. [33]. Davis et al. [36] used X-ray computed tomography to obtain the granule microstructure of α-alumina particles. Crean et al. [37] measured the intra-granular pore size and spatial and chemical maps of internal granular components using X-ray micro-computed tomography in conjunction with Raman microscopy and infrared spectroscopy.

However, all the aforementioned methods cannot capture the real-time internal structure of the object in the dynamic process taking place within seconds. Synchrotron-based X-ray imaging techniques have higher photon energy, a more sensitive detector, and more rapid acquisition of data than conventional X-ray sources and CT imaging using synchrotron radiation can be easily tailored to the sample nature and experiment needs [38, 39]. So, it can capture the images with high resolution and directly visualize the rapid granulation processes within the powder materials at high temporal and spatial resolutions (sub-micrometer spatial resolution) [40]. By analyzing the data captured with this method, the morphology and physical characteristics of the granules, such as average size, surface area, pore shape, porosity, and sphericity, can be obtained. Moreover, when the 3D view is applied to the reconstructed data, an advanced understanding and quantitative analysis of granules can be achieved.

In recent years, synchrotron-based X-ray imaging techniques have been employed in studies on mixing, segregation, and granulation. Liu et al. [21] monitored the effect of time of rotation and time of vibration on the homogeneity of binary mixtures via synchrotron X-ray

computed microtomography (SR- μ CT). In Figure 2.5, the the upper, middle, and lower levels of the container of binary mixtures were imaged by SR- μ CT.
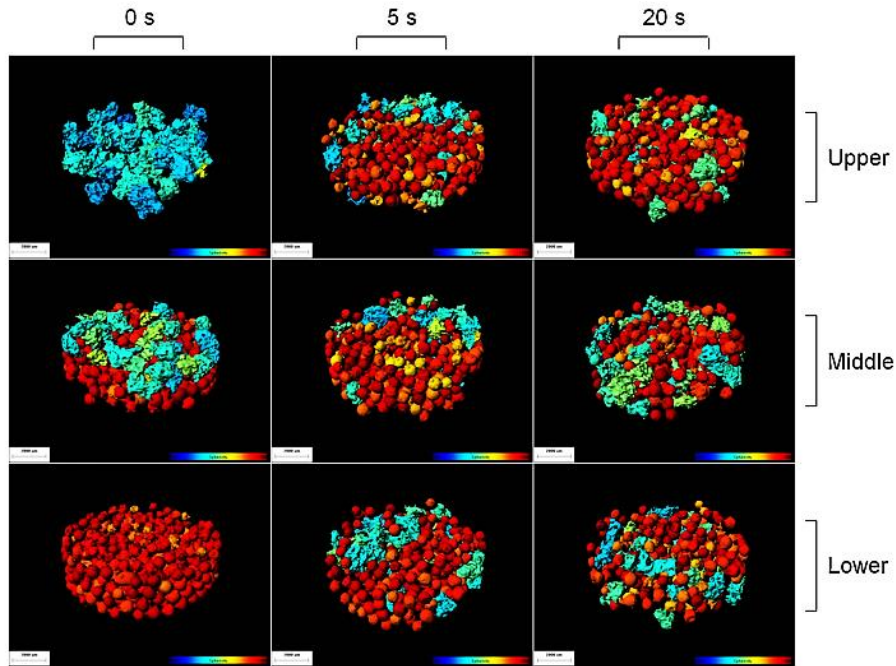
Figure 2. 5. Time of rotation impact on mixing of the granular system containing microcrystalline cellulose and starch granules [21].

Noguchi et al. [41] found CT synchrotron X-ray, a powerful method to analyze detailed internal fine granules. In their study, the spatial resolution was 0.444 μm$\times$ 0.444 μm. For objects in motion, a fast tomographic dataset is needed. Li et al. [42], for the first time, employed synchrotron-based X-ray to observe the dynamic granulation process in 2D views. By using the single-drop impact method, they compared the wetting and nucleation processes in different pharmaceutical powders (single components and mixtures). For example, Figure 2.6 demonstrates time sequence X-ray images of the dynamic wetting and nucleation process of ibuprofen (IBU) powders.
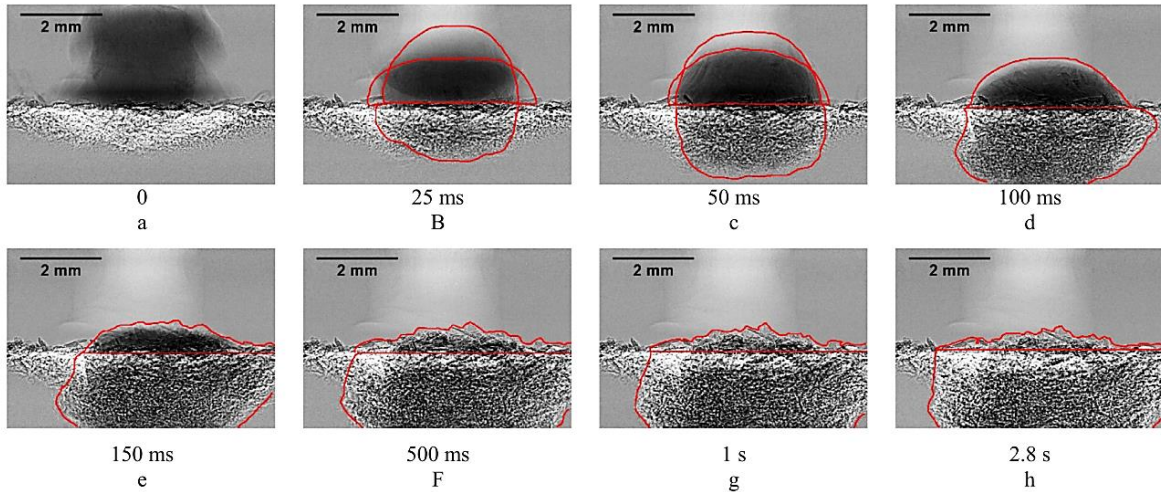
Figure 2. 6. Time-lapse images of IBU powder of dynamic wetting and nucleation process during wet granulation [42].

Wagner et al. [43] employed synchrotron phase-contrast X-ray microtomography to investigate the distribution of the pharmaceutical ingredients inside mini-tablets. They used this method to quantitatively analyze drug content and distribution within pharmaceutical tablets for the improvement of fast disintegrating formulations. Figure 2.7 shows the cross-sectional view of the tablets identifying different components based on the different grey values.
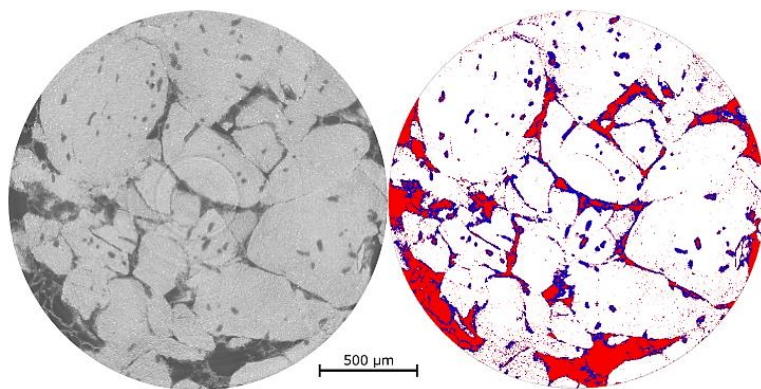
Figure 2. 7. A cross-sectional axial slice through the phase-contrast reconstructed volume of a mini-tablet. Left: Phase-contrast X-ray microtomography. Right: The clustering algorithm to distinguish the three main tablet ingredients: FCC (white), Moxidectin (red), and Croscarmellose Sodium and mixture material (MM) (blue) [43].

2.6. References

[1]   M. E. Aulton and K. M. G. Taylor, Eds., *Aulton's Pharmaceutics, The Design and Manufacture of Medicines*, Fifth. Elsevier, 2018.

[2]   M. E. Aulton, Ed., *Pharmaceutics: The Science of Dosage Form Design*, Second. Elsevier, 2002.

[3]   P. Knight, "Challenges in granulation technology," *Powder Technol.*, vol. 140, no. 3, pp. 156–162, 2004, doi: 10.1016/j.powtec.2004.01.008.

[4]   S. M. Iveson and J. D. Litster, "Fundamental studies of granule consolidation. Part 2: Quantifying the effects of particle and binder properties," *Powder Technol.*, vol. 99, no. 3, pp. 243–250, 1998, doi: 10.1016/S0032-5910(98)00116-8.

[5]   S. M. Iveson, J. D. Litster, K. Hapgood, and B. J. Ennis, "Nucleation, growth and breakage phenomena in agitated wet granulation processes: a review," *Powder Technol.*, vol. 117, no. 1, pp. 3–39, 2001, doi: https://doi.org/10.1016/S0032-5910(01)00313-8.

[6]   P. C. Knight, "Structuring agglomerated products for improved performance," *Powder Technol.*, vol. 119, no. 1, pp. 14–25, 2001, doi: 10.1016/S0032-5910(01)00400-4.

[7]   P. Suresh, I. Sreedhar, R. Vaidhiswaran, and A. Venugopal, "A comprehensive review on process and engineering aspects of pharmaceutical wet granulation," *Chem. Eng. J.*, vol. 328, pp. 785–815, 2017, doi: 10.1016/j.cej.2017.07.091.

[8]   O. R. Arndt, R. Baggio, A. K. Adam, J. Harting, E. Franceschinis, and P. Kleinebudde, "Impact of Different Dry and Wet Granulation Techniques on Granule and Tablet Properties: A Comparative Study," *J. Pharm. Sci.*, vol. 107, no. 12, pp. 3143–3152, 2018, doi: 10.1016/j.xphs.2018.09.006.

[9]   A. Faure, P. York, and R. C. Rowe, "Process control and scale-up of pharmaceutical wet granulation processes: A review," *Eur. J. Pharm. Biopharm.*, vol. 52, no. 3, pp. 269–277, 2001, doi: 10.1016/S0939-6411(01)00184-9.

[10]   H. N. Emady, D. Kayrak-Talay, and J. D. Litster, "A Regime Map for Granule Formation by Drop Impact on Powder Beds," *AIChE J.*, vol. 59, 2013, doi: 10.1002/aic.

[11]   T. Gao *et al.*, "Powder bed packing and API content homogeneity of granules in single drop granule formation," *Powder Technol.*, vol. 366, pp. 12–21, 2020, doi: 10.1016/j.powtec.2020.02.039.

[12]   T. Gao *et al.*, *Granule formation and structure from single drop impact on heterogeneous*

powder beds, vol. 552, no. 1–2. 2018.

[13]   H. N. Emady, D. Kayrak-Talay, W. C. Schwerin, and J. D. Litster, "Granule formation mechanisms and morphology from single drop impact on powder beds," *Powder Technol.*, vol. 212, no. 1, pp. 69–79, 2011, doi: 10.1016/j.powtec.2011.04.030.

[14]   H. R. Charles-Williams, R. Wengeler, K. Flore, H. Feise, M. J. Hounslow, and A. D. Salman, "Granule nucleation and growth: Competing drop spreading and infiltration processes," *Powder Technol.*, vol. 206, no. 1, pp. 63–71, 2011, doi: https://doi.org/10.1016/j.powtec.2010.06.013.

[15]   D. M. Parikh, Ed., *Handbook of pharmaceutical granulation technology*. Taylor & Francis Group, 2005.

[16]   S. M. Iveson, K. F. Rutherford, and S. R. Biggs, "Liquid penetration rate into submerged porous particles: Theory, experimental validation and implications for iron ore granulation and sintering," *Trans. Institutions Min. Metall. Sect. C Miner. Process. Extr. Metall.*, vol. 110, no. SEP./DEC., 2001, doi: 10.1179/mpm.2001.110.3.133.

[17]   A. L. Mundozah, J. J. Cartwright, C. C. Tridon, M. J. Hounslow, and A. D. Salman, "Hydrophobic/hydrophilic static powder beds: Competing horizontal spreading and vertical imbibition mechanisms of a single droplet," *Powder Technol.*, vol. 330, pp. 275–283, 2018, doi: 10.1016/j.powtec.2018.02.032.

[18]   R. P. Dias, J. A. Teixeira, M. G. Mota, and A. I. Yelshin, "Particulate binary mixtures: Dependence of packing porosity on particle size ratio," *Ind. Eng. Chem. Res.*, vol. 43, no. 24, pp. 7912–7919, 2004, doi: 10.1021/ie040048b.

[19]   X. He, X. Han, N. Ladyzhynsky, and R. Deanne, "Assessing powder segregation potential by near infrared (NIR) spectroscopy and correlating segregation tendency to tabletting performance," *Powder Technol.*, vol. 236, pp. 85–99, 2013, doi: 10.1016/j.powtec.2012.05.021.

[20]   S. Oka *et al.*, "The effects of improper mixing and preferential wetting of active and excipient ingredients on content uniformity in high shear wet granulation," *Powder Technol.*, vol. 278, pp. 266–277, 2015, doi: 10.1016/j.powtec.2015.03.018.

[21]   R. Liu *et al.*, "Visualization and quantitative profiling of mixing and segregation of granules using synchrotron radiation X-ray microtomography and three dimensional reconstruction," *Int. J. Pharm.*, vol. 445, no. 1–2, pp. 125–133, 2013, doi:

10.1016/j.ijpharm.2013.02.010.

[22] P. Tang and V. M. Puri, "Methods for minimizing segregation: A review," *Part. Sci. Technol.*, vol. 22, no. 4, pp. 321–337, 2004, doi: 10.1080/02726350490501420.

[23] S. Oka, A. Sahay, W. Meng, and F. Muzzio, "Diminished segregation in continuous powder mixing," *Powder Technol.*, vol. 309, pp. 79–88, 2017, doi: 10.1016/j.powtec.2016.11.038.

[24] K. Dries and H. Vromans, "Relationship between inhomogeneity phenomena and granule growth mechanisms in a high-shear mixer," *Int. J. Pharm.*, vol. 247, no. 1–2, pp. 167–177, 2002, doi: 10.1016/S0378-5173(02)00419-2.

[25] W. R. Ketterhagen, J. S. Curtis, C. R. Wassgren, and B. C. Hancock, "Modeling granular segregation in flow from quasi-three-dimensional, wedge-shaped hoppers," *Powder Technol.*, vol. 179, no. 3, pp. 126–143, 2008, doi: 10.1016/j.powtec.2007.06.023.

[26] P. Shenoy, M. Viau, K. Tammel, F. Innings, J. Fitzpatrick, and L. Ahrné, "Effect of powder densities, particle size and shape on mixture quality of binary food powder mixtures," *Powder Technol.*, vol. 272, no. March 2020, pp. 165–172, 2015, doi: 10.1016/j.powtec.2014.11.023.

[27] J. W. Carson, "Overcoming particle segregation in the pharmaceutical and cosmetics industries," *Drug Dev. Ind. Pharm.*, vol. 14, no. 18, pp. 2749–2758, 1988, doi: 10.3109/03639048809152046.

[28] P. M. C. Lacey, "Developments in the theory of particle mixing," *J. Appl. Chem.*, vol. 4, no. 5, pp. 257–268, 1954, doi: https://doi.org/10.1002/jctb.5010040504.

[29] M. A. Ansari and F. Stepanek, "The effect of granule microstructure on dissolution rate," *Powder Technol.*, vol. 181, no. 2, pp. 104–114, 2008, doi: 10.1016/j.powtec.2006.12.012.

[30] O. A. Odeku and O. A. Itiola, "Evaluation of the effects of khaya gum on the mechanical and release properties of paracetamol tablets," *Drug Dev. Ind. Pharm.*, vol. 29, no. 3, pp. 311–320, 2003, doi: 10.1081/DDC-120018205.

[31] C. C. Sun, "Microstructure of Tablet—Pharmaceutical Significance, Assessment, and Engineering," *Pharm. Res.*, vol. 34, no. 5, pp. 918–928, 2017, doi: 10.1007/s11095-016-1989-y.

[32] D. Markl *et al.*, "Resolving the rapid water absorption of porous functionalised calcium carbonate powder compacts by terahertz pulsed imaging," *Chem. Eng. Res. Des.*, vol. 132,

pp. 1082–1090, 2018, doi: 10.1016/j.cherd.2017.12.048.

[33] H. Nadeem and T. J. Heindel, "Review of noninvasive methods to characterize granular mixing," *Powder Technol.*, vol. 332, pp. 331–350, 2018, doi: 10.1016/j.powtec.2018.03.035.

[34] T. A. Kingston and T. J. Heindel, "Optical visualization and composition analysis to quantify continuous granular mixing processes," *Powder Technol.*, vol. 262, pp. 257–264, 2014, doi: 10.1016/j.powtec.2014.04.071.

[35] J. Imoto, S. Uchida, Y. Kashiwagura, S. Tanaka, and N. Namiki, "Morphological evaluation of low-dose midazolam granules by laser Raman microscopy," *Int. J. Pharm.*, vol. 590, no. September, p. 119940, 2020, doi: 10.1016/j.ijpharm.2020.119940.

[36] N. B. Davis, K. Waibel, K. Wang, and J. D. Litster, "Microstructure of single-droplet granules formed from ultra-fine powders," *Powder Technol.*, vol. 305, pp. 19–26, 2017, doi: 10.1016/j.powtec.2016.09.033.

[37] B. Crean *et al.*, "Elucidation of the internal physical and chemical microstructure of pharmaceutical granules using X-ray micro-computed tomography, Raman microscopy and infrared spectroscopy," *Eur. J. Pharm. Biopharm.*, vol. 76, no. 3, pp. 498–506, 2010, doi: 10.1016/j.ejpb.2010.08.006.

[38] H. Li *et al.*, "Microstructural investigation to the controlled release kinetics of monolith osmotic pump tablets via synchrotron radiation X-ray microtomography," *Int. J. Pharm.*, vol. 427, no. 2, pp. 270–275, 2012, doi: 10.1016/j.ijpharm.2012.02.017.

[39] M. Gonçalves *et al.*, "Droplet evaporation on porous fabric materials," *Sci. Rep.*, vol. 12, no. 1, pp. 1–11, 2022, doi: 10.1038/s41598-022-04877-w.

[40] C. Li, Y. Zhang, N. Zhu, H. N. Emady, and L. Zhang, "Experimental investigation of wet pharmaceutical granulation using in-situ synchrotron X-ray imaging," *Powder Technol.*, vol. 378, pp. 65–75, 2021, doi: 10.1016/j.powtec.2020.09.063.

[41] S. Noguchi *et al.*, "Investigation of internal structure of fine granules by microtomography using synchrotron X-ray radiation," *Int. J. Pharm.*, vol. 445, no. 1–2, pp. 93–98, 2013, doi: 10.1016/j.ijpharm.2013.01.048.

[42] L. Wagner-Hattler *et al.*, "Study of drug particle distributions within mini-tablets using synchrotron X-ray microtomography and superpixel image clustering," *Int. J. Pharm.*, vol. 573, no. October 2019, p. 118827, 2020, doi: 10.1016/j.ijpharm.2019.118827.

Chapter 3. 4D Study of Liquid Binder Penetration Dynamics

in Pharmaceutical Powders using Synchrotron X-ray

Micro Computed Tomography

The contents of this chapter have been accepted for publication in the International Journal of Pharmaceutics.

Contribution of the MSc student

Data analysis was performed by Sima Zeinali Danalou. Xiao Fan Ding provided assistance in synchrotron experiments and CT image reconstructions. Ning Zhu and Heather Emady offered technical support in synchrotron-related problems, and experiment design. Lifeng Zhang also provided supervision through the research. Sima Zeinali Danalou prepared the manuscript, and Lifeng Zhang provided editorial guidance.

Contribution of this chapter to the overall study

In this chapter, firstly, the static powder bed was visualized internally via synchrotron X-ray imaging. A quantitative study was performed on mixing quality and agglomerations assessment. Next, the penetration dynamics were captured via in-situ synchrotron X-ray imaging, and the interaction of liquid-solid and the effects of powder packing on penetration were studied.

3.1 Abstract

The properties of pharmaceutical powders, and the liquid binder, directly influence the penetration behavior in the wet granulation process of the pharmaceutical industry. Conventional methods encounter challenges in understanding this fast process. In this work, an emerging synchrotron-based X-ray imaging technique (having fast imaging capability) was employed to investigate the internal process from 2D and 3D to real-time (*in-situ* with *ms* time intervals) 3D (also considered

4D) perspectives. Two commonly used excipients (lactose monohydrate (LMH) and microcrystalline cellulose (MCC)) were used to make binary mixtures with acetaminophen (APAP) as the active pharmaceutical ingredient (API). Isopropanol and water were employed as liquid binders in the single droplet impact method. Results showed that for most of the mixtures, the porosity increased at higher fractions of APAP. MCC mixtures experienced less agglomeration and more uniform pore distribution than LMH ones, resulting in a faster droplet penetration with isopropanol. Moreover, the imbibition-spreading studies showed that isopropanol penetration in MCC powders followed more unidirectional vertical movement than horizontal spreading. Our results also demonstrated that simultaneous granulation of LMH with water resulted in much slower penetration. This study revealed that synchrotron X-ray imaging can investigate 3D internal pore structures and how they affect the quantitively real-time internal penetration dynamics.

Keywords: Pharmaceutical powders; wet granulation; penetration; droplet imbibition; droplet spreading; synchrotron X-ray imaging.

3.2 Introduction

Wet granulation is one of the essential unit operations in the pharmaceutical industry, by which particles agglomerate with the addition of a liquid binder. Wetting and nucleation, consolidation and growth, and attrition and breakage are the three key steps in the wet granulation process [1]. Feed powder and binder properties directly affect granulation [2]. Thus, understanding the interaction between liquid binder droplets and powder mixtures is vital for further improvements in pharmaceutical granulation.

It is well recognized that the powder mixing quality directly impacts the final products in many industries, including pharmaceuticals, cement, food, and plastics. Particle segregation is desirable in the case of separating specific components; however, it could lead to various problems. As an example, in the pharmaceutical industry, if the ratio of the active component is not the same

21

in all of Table 3.1, the desired quality of Table 3.1 would not be met, resulting in significant economic losses [3]. The physical properties, including particle size and morphology, significantly impact powder segregation [4]. Among them, the leading cause of powder segregation is particle size differences [5]. Generally, segregation is lower in cohesive powders [6]. Particles larger than 250 μm are typically free-flowing, but as the size decreases below 100 μm, powders become cohesive, and flow issues are likely (Aulton, 2002). Particle size affects cohesive interactive forces between particles related to electrostatic, van der Waals, and hydrophilic interactions [6]. As a result of decreased particle size and increasing cohesion, agglomeration occurs, which is a common phenomenon during the first stages of mixing [7].

Powder packing is another important factor affecting pharmaceutical processing and product properties. There are correlations between pore structure, bed porosity, permeability, and fluid flow or liquid mass transfer within the porous media [8]. Porosity is primarily determined by particle size, size distribution, and particle shape under specified packing circumstances. In the literature, many numerical studies have been conducted to predict powder mixtures' porosity [9]–[11]. Due to the fact that industrial powders often deviate from ideal assumptions of spherical, smooth, and solid particles, the models would not provide a reliable estimate. For example, rod-shaped, tiny, and cohesive particles would pose additional challenges to predicting their bulk behavior, such as porosity [12]. Therefore, it is imperative to develop a method to directly observe the internal structure of powders to advance knowledge on the porosity of powder mixtures with irregular particle properties.

While the droplet penetrates the powder bed, a general combination of spreading and imbibition occurs in the wetting stage of wet granulation [13]. The porosity, size, orientation of the pores, and surface chemistry within the bed all contribute to the imbibition of a single drop

into a porous substrate [2]. Different methods have been employed to study the droplet penetration phenomenon into porous media, such as optical microscopes, high-speed imaging cameras, and scanning electron microscopy (SEM). Single droplet granule formation is a promising method that has been used in many studies on droplet penetration, granule formation, and formed granules [14]–[18]. Gao et al. [15], [19] used a high-speed camera (Photron Fastcam-X 1024 PCI) to investigate granule formation mechanisms from pharmaceutical powders. Pan et al. [20] recorded water droplet imbibition into a nanoporous carbon scaffold with an environmental scanning electron microscope (ESEM) at a rate of approximately 1/3 or 3 frames per second. Hapgood et al. [2] used a Zeiss Stemi 2000 microscope with a Sony CCD camera and a JVC SVHS video recorder operating at 25 frames/s to film a single droplet penetrating into the powder. However, all mentioned techniques were not able to visualize the internal structure during the *in-situ* droplet penetration process. Studying the internal structures has received increasing attention recently, and this development was made possible by using the emerging capability of a synchrotron X-ray (e.g., higher photon flux and better light source of 3rd and 4th generation synchrotron technique, high speed detector system available, and the progress of high speed imaging processing system) to scan ultra-fast phenomena using time-resolved techniques [21]. As an example, Gonçalves et al. [22] recently used synchrotron X-ray imaging to observe water dynamics in porous and non-porous substrates and could provide a valuable framework for understanding wetting and evaporation in porous fabric substrates.

Pharmaceutical powders and droplet penetration within them, on the other hand, have rarely been investigated internally due to their opaque nature and rapid processes [23]. Synchrotron X-ray imaging overcomes the problems and limitations of the conventional methods, such as light scattering, low spatial resolution, slow imaging, and sample damage [22]. Synchrotron X-ray

imaging techniques (with a speed of approximately 2000 frames/s) allow for visualization of the powder and binder penetration inside the powder media through high-resolution 2D- and 3D-images.

The objective of this study was to employ synchrotron X-ray imaging techniques to characterize the mixing quality and 3D internal properties of the static powder bed of a model two-component system consisting of acetaminophen with microcrystalline cellulose or lactose monohydrate, mainly focusing on particle size effects. And, more specifically, this work studied how powder bed microstructures affect the internal real-time 3D (in-situ 3D imaging, or 4D) single droplet penetration dynamics by two binders of water and isopropanol.

3.3 Materials and Methods

3.3.1 Materials

Acetaminophen (APAP) as an active pharmaceutical ingredient and two commonly used excipients, microcrystalline cellulose (MCC) and lactose monohydrate (LMH), as fillers were used to prepare binary mixtures. APAP, MCC, and LMH were ordered from Hebei Jiheng Pharmaceutical, FMC BioPolymers, and Foremost Farms, respectively.

3.3.2 Characterization

The median particle size and surface mean diameter were measured by a particle size analyzer (Malvern Mastersizer 2000 S, Malvern Instruments, UK). The particle skeletal density was determined with a gas multi-pycnometer (QuantaChrome, Boynton Beach, FL, USA). A 100 mL graduated cylinder was used to measure the particle bulk density. Bulk density was calculated as the mass per unit volume, after loading the cylinder with powder through a plastic funnel at a height of 2 cm from the top of the cylinder, leveling the top surface, and then measuring the weight of the powder. The same condition was repeated for three replicates for each powder sample.

Aspect ratio (maximum width/minimum width), representing the particle morphology, was measured based on thresholding the particles in ImageJ (National Institutes of Health, USA). The microstructures of the powders were examined by SEM (Hitachi Field Emission Scanning Electron Microscope – FESEM Model SU8010, Hitachi, Japan), where the powders were precoated with a gold layer. Contact angle represents the wettability of the powder with the liquid. The contact angles are taken from our previous work and measured based on the Washburn capillary rise (WCR) method [24].

3.3.3 Sample Preparation

Firstly, to avoid large agglomerates, pure powders were sieved through a sieve with an opening size of 1 mm (US mesh # 16). To investigate the effects of powder properties on binary mixtures and droplet penetration patterns, binary mixtures were prepared with two different excipients with two particle sizes (fine and coarse). Fine lactose monohydrate (LMHF) and fine microcrystalline cellulose (MCCF) were obtained by sieving the coarse LMH and MCC powders through a sieve with a 38 μm opening size (US mesh # 400). Bulk binary mixtures were prepared with the mass fractions detailed in Table 3. 1. Binary mixtures of about 16 grams were loaded into a 10 mL vial and placed on a mixer (Fisherbrand™ Digital Vortex Mixer 80863022, Fisher Scientific) and mixed at 2000 rpm for 10 minutes. This mixing condition was fixed for all powders, and it was tested for the sample with a composition of 50LF-50A as a base model. In order to characterize mixing quality, Lacey's mixing index [25], based on the variance between the active component concentration at perfect mixing and total segregation, was employed in this work, and this mixing index (MI) is given by Equation 1:

$$MI = \frac{\sigma_0^2 - \sigma^2}{\sigma_0^2 - \sigma_r^2} \tag{1}$$

$$\sigma^2 = \frac{1}{n-1} \sum_{i=1}^{n} (x_i - \bar{x})^2 \tag{2}$$

where σ_0^2, σ^2 and σ_r^2 are the concentration variance of APAP at complete segregation, the actual mixing condition, and a random mixture in the almost completely mixed state ($\sigma_r^2 \cong 0$), respectively; n is the total sample number; x_i is the composition of APAP in the 50LF-50A mixture; and $\bar{x}$ is the mean average mass concentration of APAP. If MI is close to 1, it means the binary system experienced uniform mixing. For this purpose, 10 mg was sampled from each of the ten layers of the vial, as shown in Figure 3.1. UV–vis spectrometry was used to determine the APAP content. In the experiments, 10 mg powder was dissolved in 10 mL of deionized water (as solvent), and then 45 µL of the solution was diluted to 5 mL with deionized water (The solubility of Acetaminophen in water at 20 °C is relatively 15 mg/ml [26]). The diluted solution was assayed at 232 nm. Two trials were performed, and based on the absorbance and corresponding APAP concentrations along the vial, the MI was measured as roughly 98% for 50LF-50A for each trial.
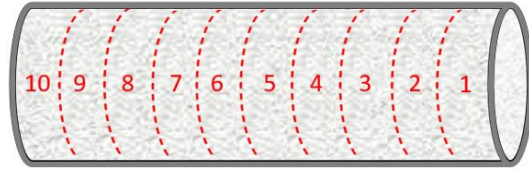
Figure 3. 1. The schematic diagram of the binary powder mixture container.

For synchrotron X-ray imaging, the powder mixture from the bulk container (16 g) was poured through a plastic funnel into a vial with a height of 2 cm and an inner diameter of 1 cm. To have a consistent pouring velocity, the funnel was positioned at a fixed height of 1 cm from the top of the vial. Prior to imaging, the powder surface was leveled to gain a smooth surface.

Table 3. 1 Mass percentage of pharmaceutical powders in binary mixtures.

Sample No.	Sample Name	Excipient	Mass Percent (%)	APAP Mass Percent (%)
1	90L-10A	LMH	90	10
2	80L-20A	LMH	80	20
3	50L-50A	LMH	50	50
4	90LF-10A	LMHF	90	10
5	80LF-20A	LMHF	80	20
6	50LF-50A	LMHF	50	50
7	90M-10A	MCC	90	10
8	80M-20A	MCC	80	20
9	50M-50A	MCC	50	50
10	90MF-10A	MCCF	90	10
11	80MF-20A	MCCF	80	20
12	50MF-50A	MCCF	50	50

3.3.4 Penetration Dynamics Measurements

While the droplet imbibes into the powder, its volume decreases. The volume remaining at the surface ($V(t)$) can be calculated by the following equation [22]:

$$V(t) = \frac{\pi r_d{}^3}{12}\left(\frac{2 - 3\cos\theta + \cos^3\theta}{\sin^3\theta}\right) \tag{3}$$

where r_d and θ are the droplet radius and the dynamic contact angle, respectively. Due to the simultaneous wetting and nucleation, at the end of penetration, $V(t)$ would not reach zero.

When a droplet comes into contact with a porous substrate, imbibition occurs by a liquid moving into the substrate. Darcy's dimensional imbibition rate was measured to describe the imbibition rate as follows [13]:

$$R_{imb} = \frac{\left(\dfrac{V_0 - V(t)}{V_0}\right)}{\left(\dfrac{D}{D_0}\right)^2} \qquad (4)$$

where D_0 and V_0 are the initial droplet width and volume, respectively, and $V(t)$ and D are the

droplet volume and width over time, respectively.

3.3.5 Synchrotron X-ray CT Setup

Synchrotron X-ray CT experiments were performed at the Biomedical Imaging and

Therapy (BMIT) Facility 05B1-1 bending magnet beamline at the Canadian Light Source (CLS),

which is a third-generation synchrotron [23]. The X-ray projections were captured by indirect

detection using a Hamamatsu AA-40 beam monitor (Hamamatsu, Japan) downstream from a 200

µm LuAG scintillator to convert X-rays transmitted from the sample to visible light, followed by

a PCO.DIMAX HS4 camera (PCO AG, Germany). A filtered white beam provided high photon

flux. The single droplet impact method was employed to study the penetration through different

powder compositions. The liquid droplet was generated using a micropipette, and its volume was

kept constant at 10 µL, and the needle's height was kept constant at 2.5 cm from the bed surface.

The number of projections per CT for scanning the static powder and capturing the penetration

process were 3000 and 500 projections, respectively. The exposure time of each projection was 1

ms. The field of view (FOV) was 11 mm x 4 mm (v x h) (see Figure 3.2), and the effective pixel

size was 5.5 µm. The schematic setup is shown in Figure 3.3.
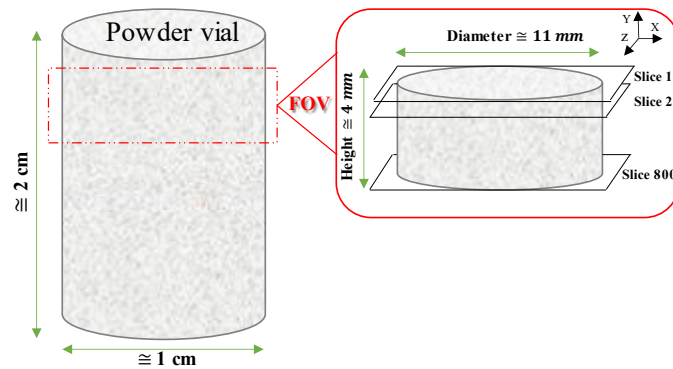
Figure 3. 2. Location and dimensions of the FOV.
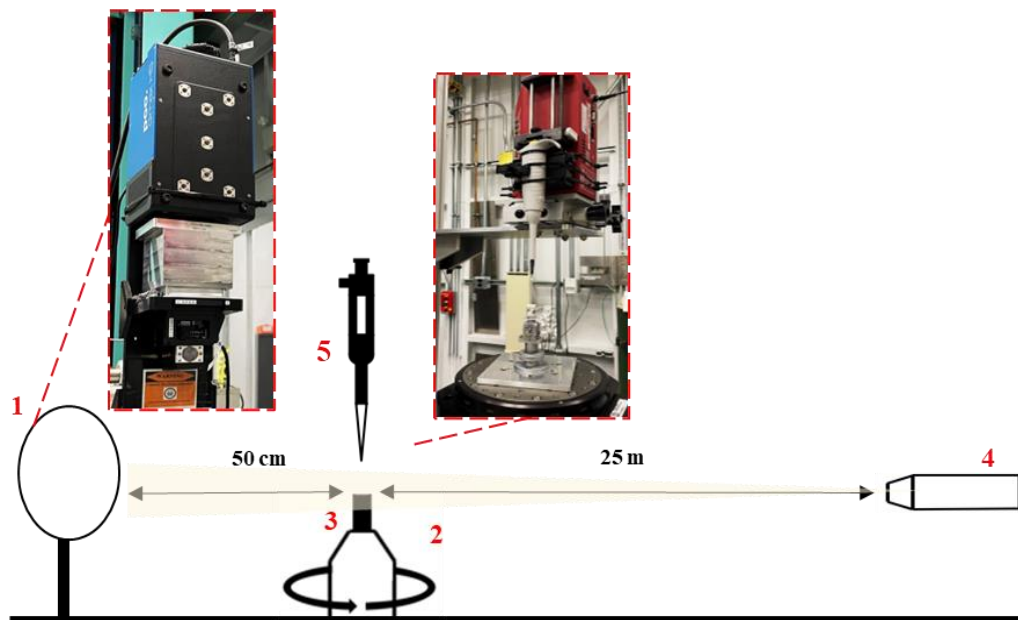
Figure 3. 3**.** Single drop experimental setup: 1) X-ray detector, 2) Rotary stage, 3) Sample vessel, 4) synchrotron X-ray beam, 5) Micropipettor and syringe pump.

3.3.6 Post-Processing and Data Analysis

UFO-KIT (Karlsruhe Institute of Technology (KIT), Germany) was used to perform tomographic reconstruction with phase retrieval [27], [28]. Two sets of images, dark and flat, were collected to spatially normalize the images without the sample. Beam and flat images were captured with a beam present, and dark images were captured without the beam. ImageJ (National Institutes of Health, USA) was used for thresholding, and Dragonfly version 2021.1 was used for

3D rendering and particle properties measurements (Objects Research Systems (ORS) Inc., Canada).

Particles with higher density absorb X-ray photons more and can be visually detected as areas with lighter grey color in the reconstructed image [29]. Hence, different gray value intensity ranges would be a common method for image segmentation. Figure 3.4 shows a cross-sectional view, in which lower gray values correspond to the area with a lower density. Consequently, air (voidage), with the lowest density compared to the solid particles, will be present in a black-dark grey color. Otsu threshold, a widely used method in image processing, in Dragonfly, was employed to segment the air voids and particles. In this approach, the histogram's mean square errors were reduced in order to choose a single threshold value. More details about this common method can be found in other publications [30], [31]. Considering the 3D volume image, the porosity was calculated by dividing the pore volume over the total volume of FOV.
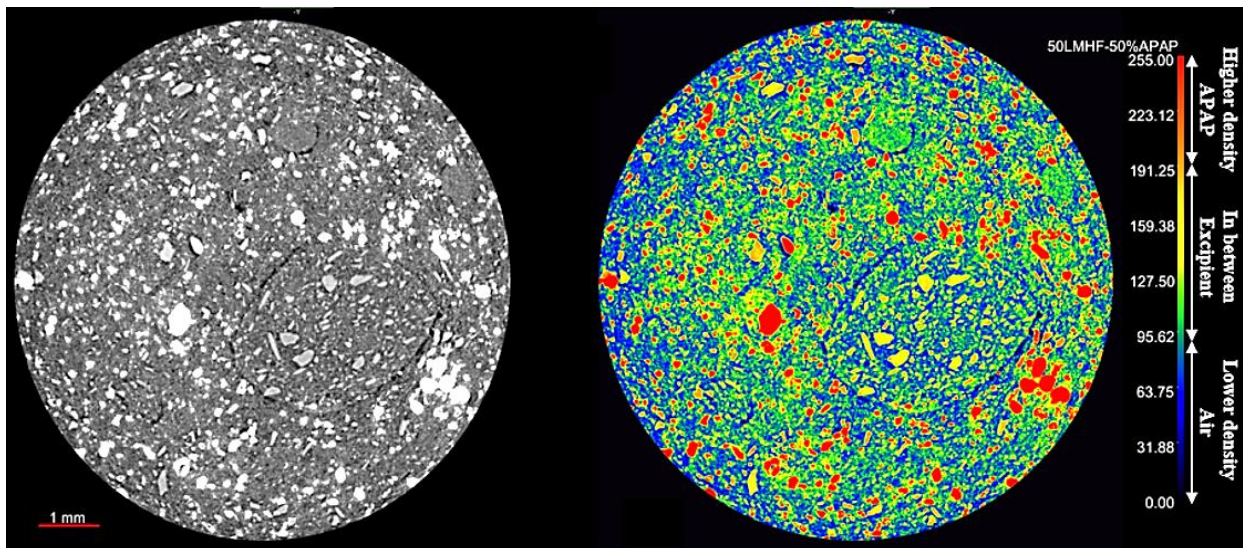
Figure 3. 4 A cross-sectional axial view of the 50LF-50A powder bed. Left: X-ray microtomography. Right: The color mapping enables the distinguishment of the three main powder components: Air with lower density (dark blue-light blue), a particle with medium density (green - orange), and a particle with higher density (red).

3.4 Results and Discussion

3.4.1. Physical Properties of Pharmaceutical Powders

Table 3. 2 presents the powder characterization, including median particle size (d_{50}), surface mean diameter (d_s), particle skeletal density (ρ_p), particle bulk density (ρ_{bed}), aspect ratio (*AR*), and contact angle with the liquid binders (isopropanol and deionized water). MCC had the largest size (110.4 µm), and LMHF had the smallest size (16.9 µm). APAP had a higher particle density compared to the excipients. Both MCC and MCCF had a higher wettability with isopropanol, and LMH had a higher wettability with water compared to LMHF. SEM images in Figure 3.5 show that APAP and MCC particles were rod-shaped with higher AR, while LMH particles showed a different morphology with lower AR.

Table 3. 2 Physical properties of pharmaceutical powders.

Powder Component	Median particle size, d_{50} (µm)	Surface mean diameter, d_s (µm)	Particle skeletal density, ρ_p (g/cm³)	Particle bulk density, ρ_{bed} (g/cm³)	Aspect ratio (AR)	Contact angle, θ (°) with isopropanol[a]	Contact angle, θ (°) with water[a]
Lactose Monohydrate (LMH)	47.9 ± 2.3	21.1	1.543±0.004	0.559	1.83	88.4±0.4	82.7 ± 0.4
Lactose Monohydrate, fine (LMHF)	16.9 ± 0.5	7.8	1.542±0.007	0.370	-	88.4±1.8	85.3 ± 2.7
Microcrystalline Cellulose (MCC)	110.4 ± 6.6	80.8	1.555±0.009	0.326	2.45	82.2. ±1.8	-
Microcrystalline Cellulose, fine (MCCF)	31.8 ± 0.1	24.6	1.556±0.010	0.343	-	57.9±3.9	-
Acetaminophen (APAP)	50.9 ± 3.9	17.1	1.701±0.001	0.539	2.59	87.5±0.4	-

[a][24]
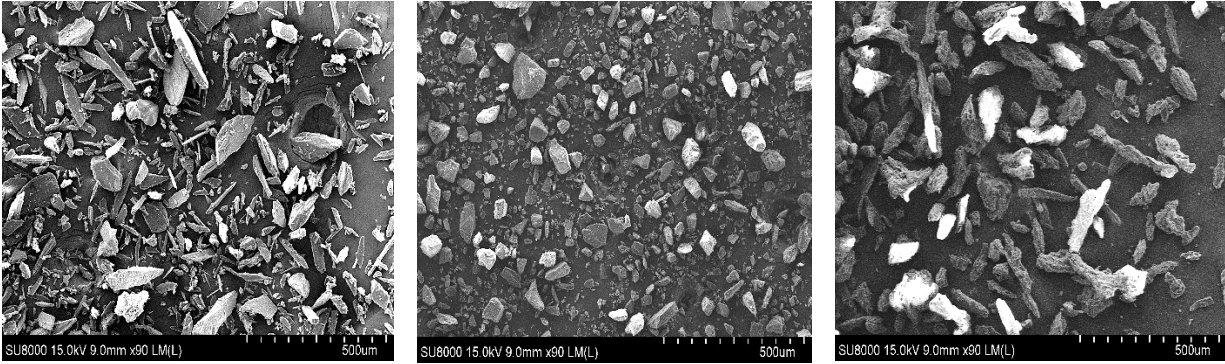
Figure 3. 5 SEM images of powders: (a) APAP, (b) LMH, and (c) MCC.

3.4.2 Static Powder Beds

3.4.2.1 Powder Porosity

Figure 3.6 shows porosity values for different powder mixtures. The porosity of a powder bed is affected by the following factors: particle size, morphology, texture, spatial distribution, bulk density, and processing conditions [5]. Particle size differences in binary mixtures play a vital role in porosity [8]. Among different powders investigated in this work, LMH and APAP have very close particle sizes and bulk densities (higher compared to others), so the particles properly fill the pores, and thus by increasing the APAP content, the porosity was found to decrease. LMHF-APAP binary mixtures had higher porosities compared to those for LMH-APAP binary mixtures. In LMHF mixtures, there are some discrete local dense areas, resulting in a porosity increase. Because the inter-particle attractive forces can prevent tiny dry particles (usually <100 μm) from moving freely, agglomerates will be formed, resulting in a porosity increase [32]. Due to the similar sizes of MCC-APAP and MCCF-APAP, similar porosities were observed. MCCF had a slightly higher bulk density and made powder beds with lower porosities. In general, for particles of different sizes, there is an additional void space between different particles [33]. As a result, by increasing the portion of the active component (reaching 50%), the porosity is expected to increase;

32

this was more obvious in the case of LMHF-APAP, as increasing the APAP fraction resulted in significantly higher porosity.
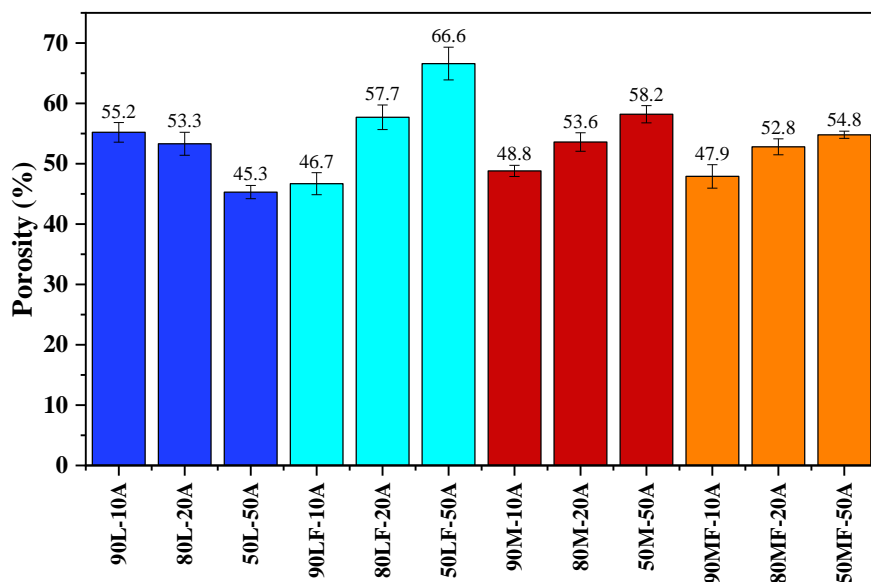
Figure 3. 6. Measured porosity for different powder compositions. (dark blue) LMH mixtures; (light blue) LMHF mixtures; (red) MCC mixtures; (orange) MCCF mixtures. (averages with standard deviations for two replicates for each mixture)

3.4.2.2 Particles Distribution along Axes and Agglomeration Status

Figure 3.7 shows the percent of area occupied by API and excipients along the Y and Z directions. Showing how much of the area is covered by a specific particle at any distance from the green origin indicated in Figure 3.7, along the height or diameter of the powder bed in FOV. The zero values in the plots (Figure 3.7a) indicate the air space at the top of the powder. According to the plots along the Y direction (Figure 3.7b), there were more pores available near the wall than in the center, which was more dominant in mixtures of fine powders.

In general, smoother trends with fewer fluctuations represented less agglomeration inside the powder bed, so the agglomeration possibility in a lower percentage of APAP (10%) was less in both coarse and fine particles. Because of the effects of inter-particle forces, agglomeration increased in all samples as the active component was increased. Overall, in accordance with

previous studies [7], [34], agglomeration increased when switching from coarse to fine particles. As a result, macro voids formed within the fine powders, as demonstrated by 90% LMHF (See Figure 3.7a). Also, agglomeration was less in MCC mixtures than in other compositions, mainly due to the better flowability of MCC particles.
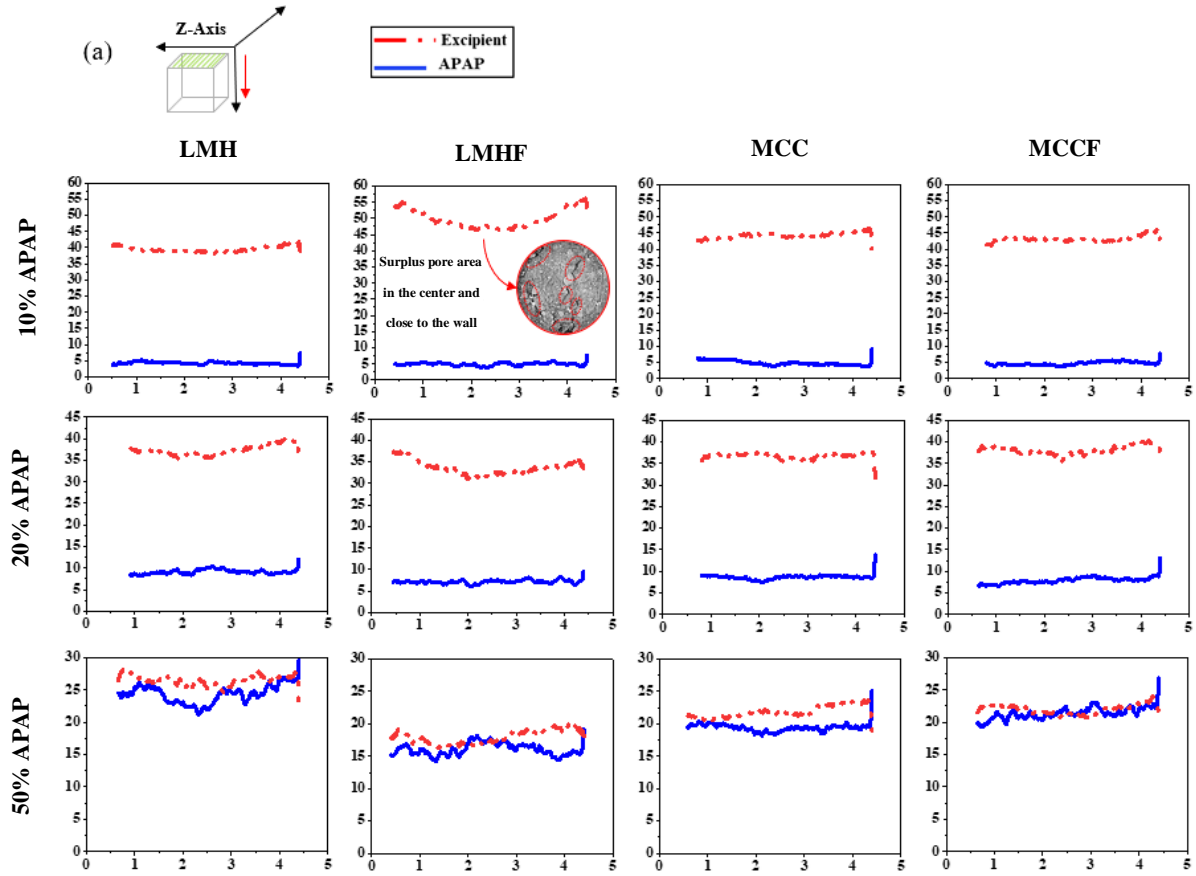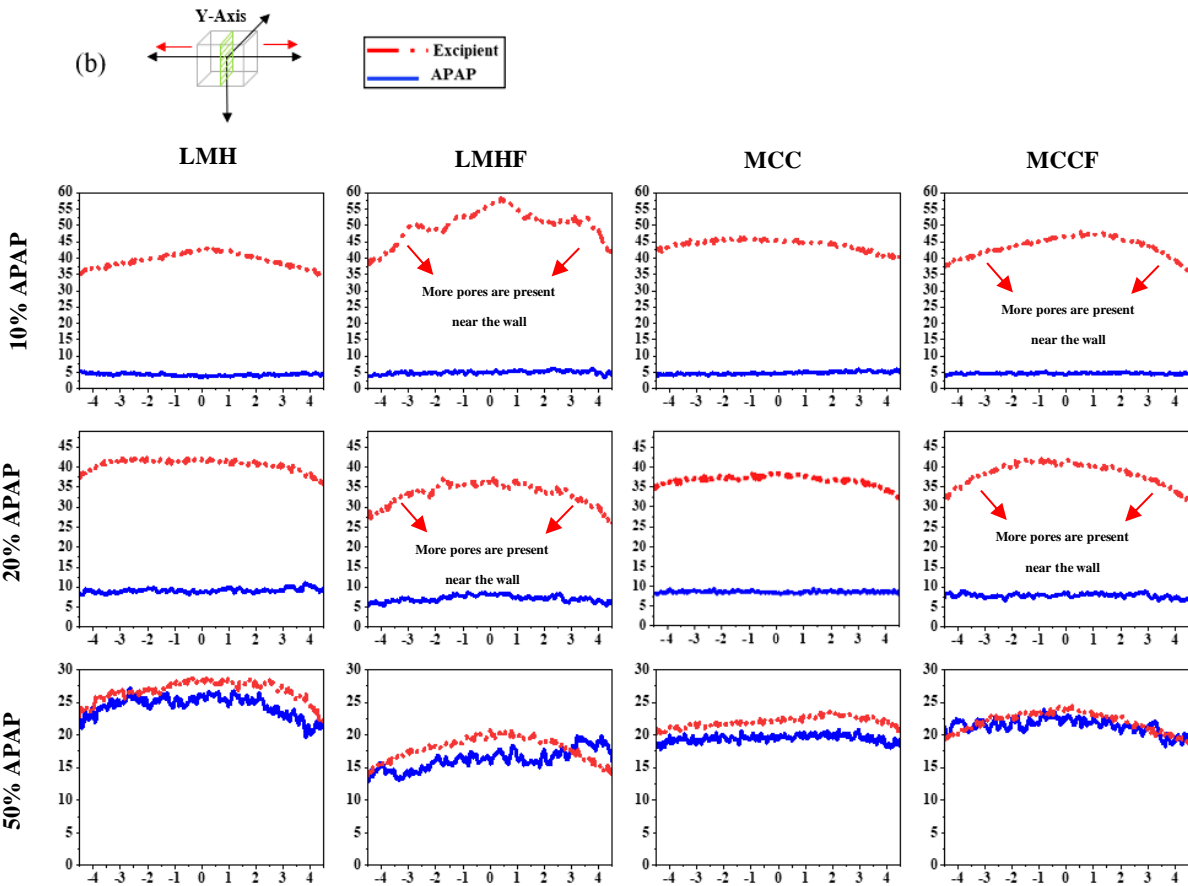
Figure 3. 7. Area percentage of different particles at different distances from the origin of volume for different compositions. (a) along Z, (b) along Y. Y-axis: Particles content (%), X-Axis: Distance from the origin (mm).

In a batch mixing process, blend homogeneity is dependent on blending time and types of excipients [35]. Powder uniformity was quantified by determining the drug content (data derived from Figure 3.7a) through 800 slices along Z in the FOV (see Figure 3.2). The relative standard deviation (RSD) over average drug concentration was measured to determine the powder uniformity along Z. A lower RSD indicates a better mixing quality in the powder.

The RSD values of the API concentration for different powder compositions are shown in Figure 3.8. Generally, at a lower fraction of APAP, a lower mixing quality was achieved [36]. 90M-10A had the largest RSD value, as MCC and APAP had different particle sizes and shapes.

In contrast, at 50% of the excipients, MCC and MCCF mixtures contributed to better mixing quality. The reason is due to the tendency for agglomeration in LMH and LMHF mixtures (see Figure 3.7a), which is a common type of segregation in powder technology [37].
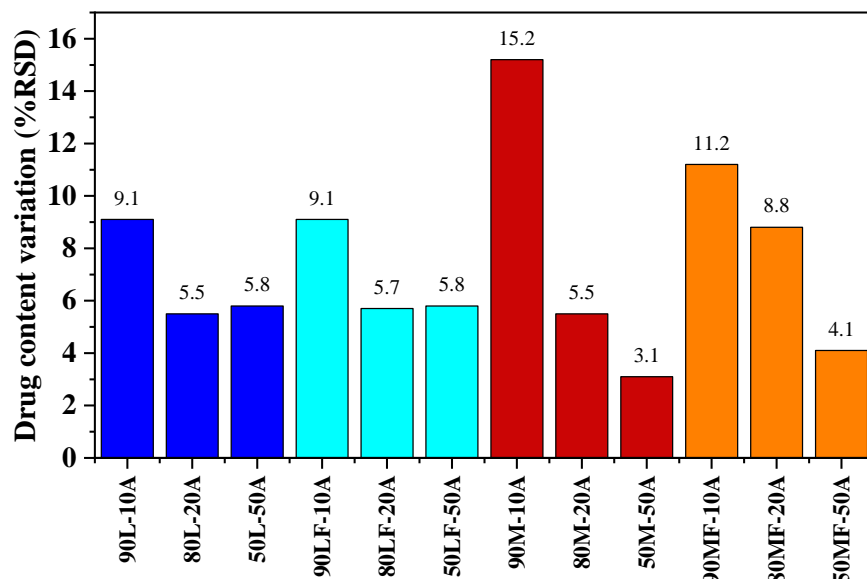
Figure 3. 8**.** RSD represents binary mixtures' uniformity. (dark blue) LMH mixtures; (light blue) LMHF mixtures; (red) MCC mixtures; (orange) MCCF mixtures.

3.4.3 Penetration Dynamics

Both 2D radiography and 3D microtomography techniques were applied to visualize liquid binder droplet penetration inside the powder bed. Figure 3.9 illustrates the granulation procedure in the spray zone in the wet granulator, and due to the very fast first steps and artifacts problem, 2D images are used for illustration. This study focuses on the droplet penetration stage (Figure 3.9 c).
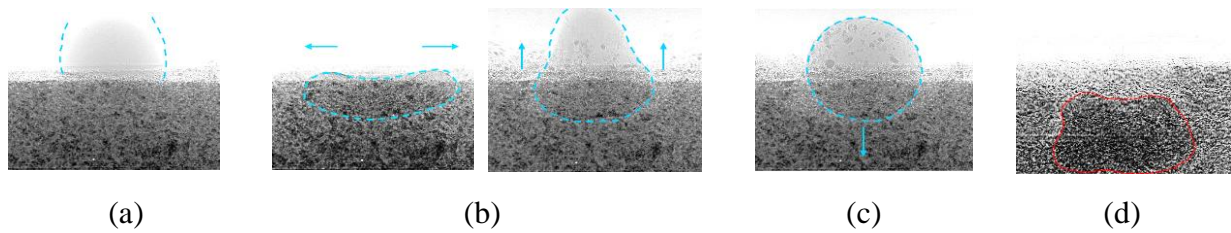
Figure 3. 9 The four steps of granulation. The droplet is indicated with a blue dashed line, and the final granule is shown by a red dashed line (the wet final granule, as a denser area, is darker compared to the surroundings). (a) droplet impact; (b) droplet spreading and rebound; (c) droplet penetration into the powder pores and wetting; (d) nucleation and granule formation.

A 50% excipient fraction was set for different powders. Because the penetration of 50M-50A with deionized water occurred in less than 200 ms, there were too many artifacts preventing a good analysis, so 50LF-50A and 50L-50A were chosen to compare the two binders. Based on the experiments, for most powder cases, the granulation took place simultaneously while the droplet was penetrating, so penetration time in this study was defined as the time from the beginning of the penetration (Figure 3.9c) to the point that the contact angle remained unchanged and the droplet height was positive based on the defined base. Due to the porous nature of the powder bed and the velocity and weight of the droplet, after the first impact of the droplet, there was a crater formed on the powder surface (see Figure 3.10), but after that, the surface was pinned during the penetration. To relate the powder bed structural properties and the droplet spreading and imbibition behavior, droplet width (D), maximum droplet height (H), and dynamic contact angle (θ) with time were measured (see Figure 3.10). To be consistent in the measurements, the base was set for each composition, considering the image sequences and final granule status (red dashed line in Figure 3.10).

(a)   (b)
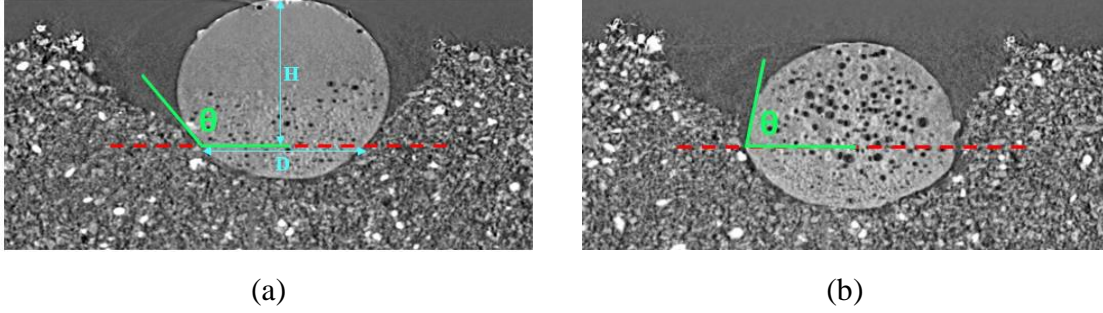
Figure 3. 10**.** Illustration of droplet penetration parameters, 50L-50A with deionized water. The red dashed line is the base, where droplet and powder contact ends. (a) during the penetration, (b) endpoint.

Different powders had different ranges for the penetration parameters. The time was normalized by t^*, corresponding to the time the penetration process finished. Droplet and height evolution and contact angle decay were normalized with respective initial values. So, in order to compare the imbibition/spreading behavior of the droplet, some dimensionless parameters were defined as below:

$$\bar{t} = \frac{t}{t^*} \tag{5}$$

$$\bar{D} = \frac{D}{D_0} \tag{6}$$

$$\bar{H} = \frac{H}{H_0} \tag{7}$$

$$\bar{\theta} = \frac{\theta}{\theta_0} \tag{8}$$

where t^*, D_0, H_0 and θ_0 are final penetration time, initial droplet width, initial droplet height from the bed surface, and initial contact angle, respectively. The summary of penetration parameters for different powders is provided in Table 3. 3. The parameters include penetration time, t^*, maximum spreading width, which is the maximum droplet width, D_M, and maximum contact angle, θ_M.

Table 3. 3 Penetration properties.

Powder	Binder	Sample name	Penetration time, t^*(s)	Penetration length, L (mm)	Maximum spreading width, D_M (mm)	Maximum contact angle, θ_M (°)
50L-50A	Isopropanol	50L-50A-I	5.10	0.69	3.05	124
50LF-50A	Isopropanol	50LF-50A-I	5.00	0.78	3.23	125
50M-50A	Isopropanol	50M-50A-I	0.27	0.81	2.94	97
50MF-50A	Isopropanol	50MF-50A-I	0.85	1.01	3.15	125
50L-50A	Deionized water	50L-50A-W	870	1.07	3.05	125
50LF-50A	Deionized water	50LF-50A-W	1,110	1.24	2.77	127

LMH and LMHF had a larger static contact angle with isopropanol than those for MCC and MCCF, as well as fewer uniform particles and less uniform pore distribution (see Figure 3.7), and these properties prevented the droplet from penetrating [2]. As such, the droplet penetrated much more slowly with a shorter penetration length. Figure 3.11 shows a clear visualization of the dynamic droplet penetration. These images are cross-sectional views from a 3D volume.
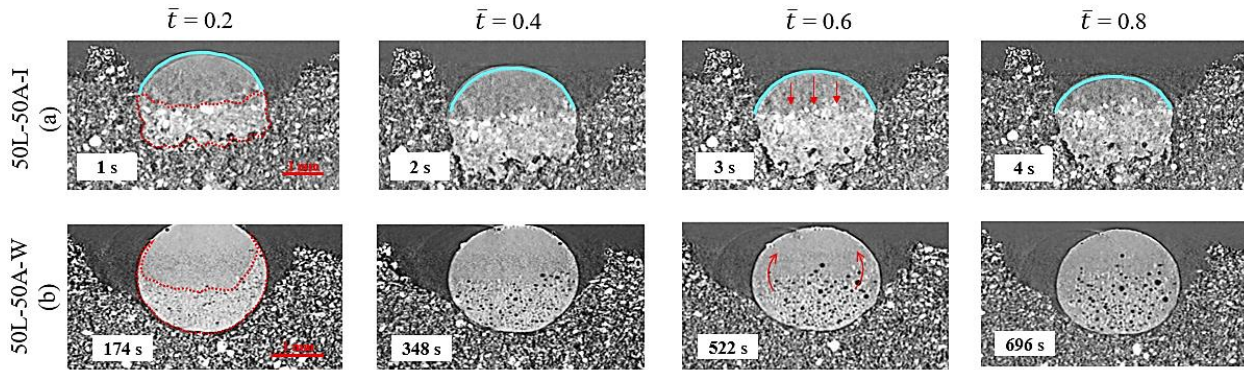
Figure 3. 11. Time CT images of the droplet penetration at time points $\bar{t}$ = 0.2, 0,4, 0.6, and 0.8. (a) 50L-50A with isopropanol, droplet cap is shown by a blue line and the granule is forming beneath the bed surface. (b) 50L-50A with deionized water, powder covers the droplet and moves inward to form the granule.

Porosity had a greater impact on the penetration time than the static contact angle with the liquid binder, according to Shi et al. [38]. Both LMHF and LMH had the same contact angle with isopropanol, but 50LF-50A had a higher porosity than 50L-50A (see Figure 3.6), resulting in a

shorter penetration time. Agglomeration and non-uniformity of the powder bed were other significant factors affecting the penetration time. As shown in Figure 3.7, the 50MF-50A sample with less uniformity and a lower porosity than that of 50M-50A had a longer penetration time. Both 50LF-50A and 50L-50A had a much longer penetration time with water than isopropanol. LMH was soluble in water [13], and partial dissolution and intermediate viscous forces slowed down the imbibition considerably. The presence of powders on the droplet surface and simultaneous dominant nucleation (see Figure 3.11b) prevented the droplet from penetration, so internal porosity did not play an important role. In addition, as LMHF had a higher contact angle with water compared to LMH, the penetration/granulation process of the LMHF powders was longer.

3.4.3.1 Droplet Geometry

To compare the droplet shape evolution with time, changes in its width and height were normalized over time, and are shown in Figure 3.12.
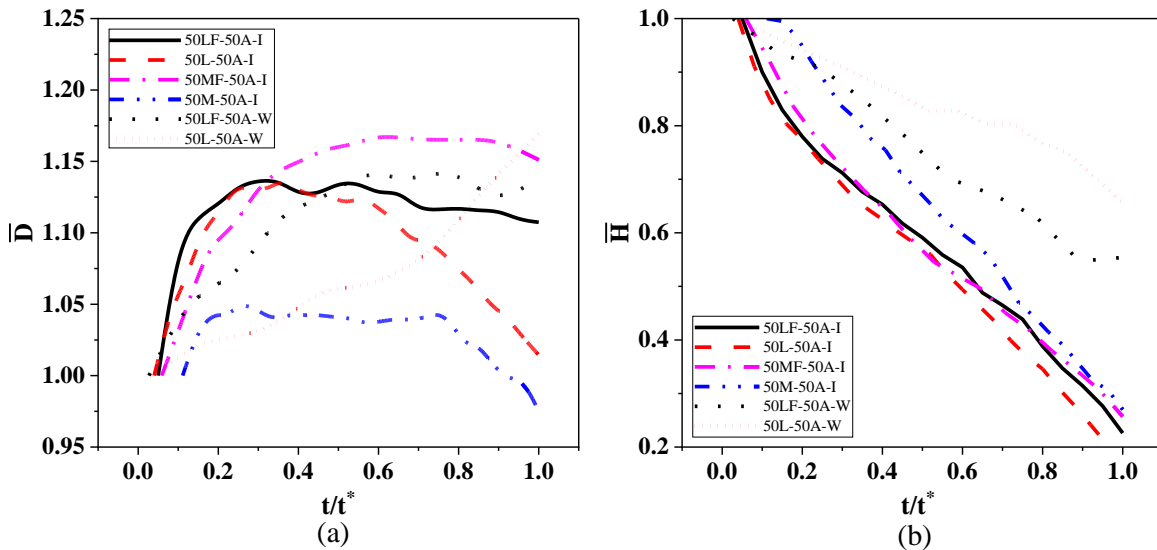
Figure 3. 12. Droplet width and height dynamics as a function of time. (a) dimensionless droplet width, (b) dimensionless droplet height.

The changes in the droplet width were minimal (Figure 3.12a), with the greatest change being a 17% increase in 50L-50A-W. And, because the changes were small, the droplet width was assumed to remain constant during the penetration. Both fine and coarse powders with the same binder showed very similar behavior regarding the droplet width evolution.

As mentioned earlier, the droplet height was smoothly reduced due to the uniform pore distribution of the MCC powders. In contrast, particularly in LMH and LMHF, the droplet height (isopropanol) initially decreased at a faster rate, which could be attributed to the presence of larger pores at the beginning of the droplet path, thereby enhancing flow [13]. The lower $\bar{H}$ ratio at the end indicates that a significant amount of the droplet was absorbed after the first impact, which could be due to the pore structure or a lower static contact angle (higher wettability with the binder), which can be seen in MCC and MCCF mixtures. Both LMH and LMHF with water showed different penetration patterns from all isopropanol compositions. From the first impact of the droplet, powders attach to the droplet surface (see Figure 3.11b). Therefore, because of the simultaneous wetting and nucleation, the droplet height did not change noticeably. As a result, there was no significant imbibition. However, these droplets tended to spread horizontally (see Figure 3.12a).

3.4.3.2 Dynamic Droplet Volume and Contact Angle

Figure 3.13a shows the volume changes of a droplet before complete imbibition. Volume changes for MCC-MCCF follow the $\sqrt{t}$ trend based on single-phase Darcy's law, which assumes a 1D flow [39]. However, liquid droplet penetration is a 3D process [13]. It can be concluded that for MCC-MCCF mixtures, as the power values were closer to 0.5, during the penetration, the droplet tended to imbibe rather than spread, which was in agreement with the uniform pore distribution inside the powder (see Figure 3.7). In addition, due to the MCC-MCCF structure (see

Figure 3.4), rod-shaped pores were present as well, enhancing the vertical flow [38]. For 50LF-50A-W and 50L-50A-W, *V(t)* remained high due to negligible imbibition and dominant granulation into the droplet from its surface. The power values (low and around 0.2) for power laws deviated greatly with the single-phase Darcy's law, implying a very slow or no imbibition into the powder bed.

The dynamic contact angle decreased for all compositions, as clearly shown in Figure 3.13b. As there was no significant penetration for 50LF-50A-W and 50L-50A-W, the contact angle did not change much either. While the droplet is penetrating, its width and contact angle change, and the penetration takes place in three probable mechanisms, constant drawing area (CDA), decreasing drawing area (DDA), and increasing drawing area (IDA) [13], [40]. It can be concluded that the droplet penetration inside all powders is described above in the CDA phase, where the dynamic contact angle decreased while the droplet width remained constant [13].
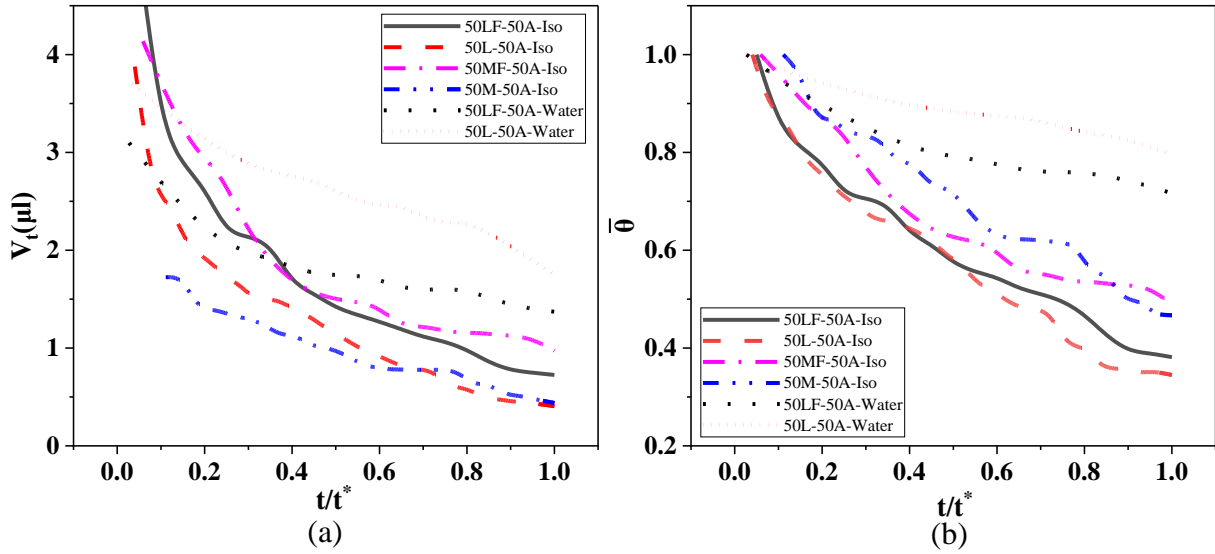
Figure 3. 13. Droplet volume and contact angle dynamics as a function of time. (a) the volume of droplet remained on the surface and the corresponding power-law fits are as follows: (solid) $y = 0.834x^{-0.689}$, $R^2 = 0.936$; (dash) $y = 0.5606x^{-0.711}$, $R^2 = 0.9015$; (dash dot) $y = 1.0433x^{-0.553}$, $R^2 = 0.9352$; (dash dot dot) $y = 0.5715x^{-0.606}$, $R^2 = 0.9059$; (dot) $y = 1.4675x^{-0.229}$, $R^2 = 0.9655$; (short dot) $y = 2.1609x^{-0.186}$, $R^2 = 0.851$. (b) dimensionless dynamic contact angle.

3.4.3.3 Vertical Imbibition

In all compositions, the gradual rate of imbibition increased (see Figure 3.14). Finer particles had a slower imbibition rate, because of the aggregation of fine particles and the presence of local packings and macropores hindering the penetration process. Tortuosity increases when the porosity decreases [41]. When compared to others, 50M-50A had higher porosity, which resulted in higher permeability, increased capillary suction, a faster imbibition rate, and a shorter penetration time. Based on the competing imbibition and spreading behavior of droplets, 50MF-50A had almost constant R_{imb} but the greatest changes in the droplet width.

43
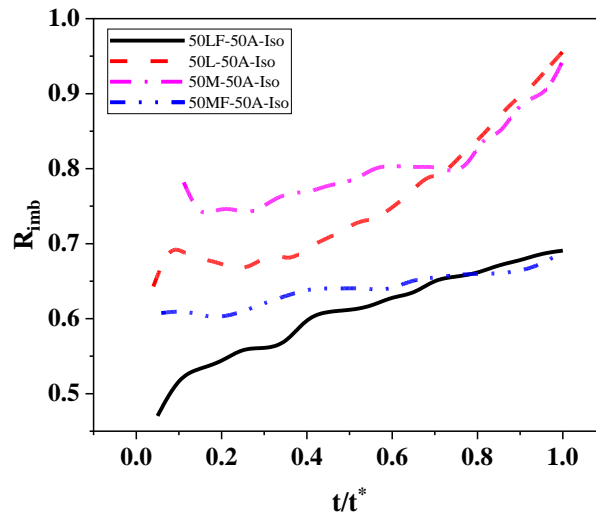
Figure 3. 14. Imbibition kinetics in dimensionless Darcy's flow.

3.5 Conclusions

This work employed an advanced synchrotron-based X-ray CT technique to investigate the pore structures and dynamic binder droplet penetration in pharmaceutical powders. In the first phase, for powder binary mixtures of LMH and MCC with APAP, the porosity, mixing quality, particles, and pore distribution along different axes were studied. Both coarse and fine excipients with mass fractions of 90%, 80%, and 50% were examined. The lower size ratios between components resulted in lower porosities, which was the case for mixtures of LMH. And, for the particles with different sizes, the porosity increased by increasing the amount of one of the components, resulting in the presence of additional void space. MCC powders were found to have less agglomeration and more uniform particle distribution. By increasing the APAP fraction, a better mixing quality was achieved. 50% of excipients were set to study the penetration dynamics with the binder of isopropanol and deionized water. Better pore distribution in the path of the droplet penetration was one dominant factor for faster penetration time and shorter penetration length. Also, higher porosity resulted in more rapid penetration, as LMHF mixtures had higher porosity than LMH ones, so the droplet penetrated faster. During penetration for all compositions,

the dynamic contact angle decreased. There was a competing behavior between spreading and imbibition of a droplet during the penetration process; as for MCCF, the imbibition rate was almost constant, but the droplet width changed more significantly, with a 15% increase. Both LMH and LMHF showed a different pattern with water; granulation was dominant over penetration because of the particle dissolution inside water.

This study demonstrated that internal observation of the powder bed and visualization of the real-time wetting provide reliable information to select the desired conditions and materials for wet granulation.

3.6 Acknowledgments

3.7 References

[1]   S. M. Iveson, J. D. Litster, K. Hapgood, and B. J. Ennis, "Nucleation, growth and breakage phenomena in agitated wet granulation processes: a review," *Powder Technol.*, vol. 117, no. 1, pp. 3–39, 2001, doi: https://doi.org/10.1016/S0032-5910(01)00313-8.

[2]   K. P. Hapgood, J. D. Litster, S. R. Biggs, and T. Howes, "Drop penetration into porous powder beds," *J. Colloid Interface Sci.*, vol. 253, no. 2, pp. 353–366, 2002, doi: 10.1006/jcis.2002.8527.

[3]   M. Asachi, E. Nourafkan, and A. Hassanpour, "A review of current techniques for the evaluation of powder mixing," *Adv. Powder Technol.*, vol. 29, no. 7, pp. 1525–1549, 2018, doi: 10.1016/j.apt.2018.03.031.

[4]   S. Oka, A. Sahay, W. Meng, and F. Muzzio, "Diminished segregation in continuous powder mixing," *Powder Technol.*, vol. 309, pp. 79–88, 2017, doi: 10.1016/j.powtec.2016.11.038.

[5]   M. E. Aulton, Ed., *Pharmaceutics: The Science of Dosage Form Design*, Second. Elsevier, 2002.

[6]   R. Furukawa *et al.*, "Size-induced segregation during pharmaceutical particle die filling assessed by response surface methodology using discrete element method," *J. Drug Deliv. Sci. Technol.*, vol. 35, pp. 284–293, 2016, doi: 10.1016/j.jddst.2016.08.004.

[7]   H. J. Venables and J. I. Wells, "Powder mixing," *Drug Dev. Ind. Pharm.*, vol. 27, no. 7, pp. 599–612, 2001, doi: 10.1081/DDC-100107316.

[8]   R. P. Dias, J. A. Teixeira, M. G. Mota, and A. I. Yelshin, "Particulate binary mixtures: Dependence of packing porosity on particle size ratio," *Ind. Eng. Chem. Res.*, vol. 43, no. 24, pp. 7912–7919, 2004, doi: 10.1021/ie040048b.

[9]   A. Clarke, T. D. Blake, K. Carruthers, and A. Woodward, "Spreading and imbibition of liquid droplets on porous surfaces," *Langmuir*, vol. 18, no. 8, pp. 2980–2984, 2002, doi: 10.1021/la0117810.

[10]   L. Forny, A. Marabi, and S. Palzer, "Wetting, disintegration and dissolution of agglomerated water soluble powders," *Powder Technol.*, vol. 206, no. 1–2, pp. 72–78, 2011, doi: 10.1016/j.powtec.2010.07.022.

[11]   F. Fu, P. Li, K. Wang, and R. Wu, "Numerical Simulation of Sessile Droplet Spreading and Penetration on Porous Substrates," *Langmuir*, vol. 35, no. 8, pp. 2917–2924, 2019, doi: 10.1021/acs.langmuir.8b03472.

[12]   X. He, X. Han, N. Ladyzhynsky, and R. Deanne, "Assessing powder segregation potential by near infrared (NIR) spectroscopy and correlating segregation tendency to Table 3.tting performance," *Powder Technol.*, vol. 236, pp. 85–99, 2013, doi: 10.1016/j.powtec.2012.05.021.

[13] A. L. Mundozah, J. J. Cartwright, C. C. Tridon, M. J. Hounslow, and A. D. Salman, "Hydrophobic/hydrophilic static powder beds: Competing horizontal spreading and vertical imbibition mechanisms of a single droplet," *Powder Technol.*, vol. 330, pp. 275–283, 2018, doi: 10.1016/j.powtec.2018.02.032.

[14] H. N. Emady, D. Kayrak-Talay, and J. D. Litster, "A Regime Map for Granule Formation by Drop Impact on Powder Beds," *AIChE J.*, vol. 59, 2013, doi: 10.1002/aic.

[15] T. Gao *et al.*, "Powder bed packing and API content homogeneity of granules in single drop granule formation," *Powder Technol.*, vol. 366, pp. 12–21, 2020, doi: 10.1016/j.powtec.2020.02.039.

[16] T. Gao *et al.*, *Granule formation and structure from single drop impact on heterogeneous powder beds*, vol. 552, no. 1–2. 2018.

[17] H. N. Emady, D. Kayrak-Talay, W. C. Schwerin, and J. D. Litster, "Granule formation mechanisms and morphology from single drop impact on powder beds," *Powder Technol.*, vol. 212, no. 1, pp. 69–79, 2011, doi: 10.1016/j.powtec.2011.04.030.

[18] H. R. Charles-Williams, R. Wengeler, K. Flore, H. Feise, M. J. Hounslow, and A. D. Salman, "Granule nucleation and growth: Competing drop spreading and infiltration processes," *Powder Technol.*, vol. 206, no. 1, pp. 63–71, 2011, doi: https://doi.org/10.1016/j.powtec.2010.06.013.

[19] T. Gao *et al.*, "Granule formation and structure from single drop impact on heterogeneous powder beds," *Int. J. Pharm.*, vol. 552, no. June, pp. 56–66, 2018, doi: 10.1016/j.ijpharm.2018.09.036.

[20] B. Pan, C. R. Clarkson, M. Atwa, C. Debuhr, A. Ghanizadeh, and V. I. Birss, "Wetting dynamics of nanoliter water droplets in nanoporous media," *J. Colloid Interface Sci.*, vol. 589, pp. 411–423, 2021, doi: 10.1016/j.jcis.2020.12.108.

[21] F. Marone *et al.*, "Time Resolved in situ X-Ray Tomographic Microscopy Unraveling Dynamic Processes in Geologic Systems," *Front. Earth Sci.*, vol. 7, 2020, doi: 10.3389/feart.2019.00346.

[22] M. Gonçalves *et al.*, "Droplet evaporation on porous fabric materials," *Sci. Rep.*, vol. 12,

no. 1, pp. 1–11, 2022, doi: 10.1038/s41598-022-04877-w.

[23]   C. Li, N. Zhu, H. N. Emady, and L. Zhang, "Synchrotron-based X-ray in-situ imaging techniques for advancing the understanding of pharmaceutical granulation," *Int. J. Pharm.*, vol. 572, p. 118797, 2019, doi: https://doi.org/10.1016/j.ijpharm.2019.118797.

[24]   C. Li, Y. Zhang, N. Zhu, H. N. Emady, and L. Zhang, "Experimental investigation of wet pharmaceutical granulation using in-situ synchrotron X-ray imaging," *Powder Technol.*, vol. 378, pp. 65–75, 2021, doi: 10.1016/j.powtec.2020.09.063.

[25]   P. M. C. Lacey, "Developments in the theory of particle mixing," *J. Appl. Chem.*, vol. 4, no. 5, pp. 257–268, 1954, doi: https://doi.org/10.1002/jctb.5010040504.

[26] R. A. Granberg and C. Rasmuson, "Solubility of Paracetamol in Pure Solvents," Chem. Eng. J. J., vol. 44, pp. 1391–1395, 1999.

[27]   M. Vogelgesang *et al.*, "Real-time image-content-based beamline control for smart 4D X-ray imaging," *J. Synchrotron Radiat.*, vol. 23, pp. 1254–1263, 2016, doi: 10.1107/S1600577516010195.

[28]   T. Faragó *et al.*, " Tofu : a fast, versatile and user-friendly image processing toolkit for computed tomography ," *J. Synchrotron Radiat.*, vol. 29, no. 3, pp. 916–927, 2022, doi: 10.1107/s160057752200282x.

[29]   W. A. Kalender, *Computed tomography Fundamentals, System Technology, Image Quality, Applications*, vol. 4, no. 1. Publicis Publishing, Erlangen, 2011.

[30]   L. Jianzhuang, L. Wenqing, and T. Yupeng, "Automatic thresholding of gray-level pictures using two-dimension Otsu method," in *China., 1991 International Conference on Circuits and Systems*, 1991, pp. 325–327 vol.1, doi: 10.1109/CICCAS.1991.184351.

[31]   N. Otsu, "A Threshold Selection Method from Gray-Level Histograms," *IEEE Trans. Syst. Man. Cybern.*, vol. 9, no. 1, pp. 62–66, 1979, doi: 10.1109/TSMC.1979.4310076.

[32]   M. Capece *et al.*, "Prediction of porosity from particle scale interactions: Surface modification of fine cohesive powders," *Powder Technol.*, vol. 254, pp. 103–113, 2014, doi: 10.1016/j.powtec.2014.01.006.

[33] A. El-Husseiny, T. Vanorio, and G. Mavko, "Predicting porosity of binary mixtures made out of irregular nonspherical particles: Application to natural sediments," *Adv. Powder Technol.*, vol. 30, no. 8, pp. 1558–1566, 2019, doi: 10.1016/j.apt.2019.05.001.

[34] B. Chaudhuri, A. Mehrotra, F. J. Muzzio, and M. S. Tomassone, "Cohesive effects in powder mixing in a tumbling blender," *Powder Technol.*, vol. 165, no. 2, pp. 105–114, 2006, doi: 10.1016/j.powtec.2006.04.001.

[35] M. Jaspers *et al.*, "Batch versus continuous blending of binary and ternary pharmaceutical powder mixtures," *Int. J. Pharm. X*, vol. 4, 2022, doi: 10.1016/j.ijpx.2021.100111.

[36] S. Oka *et al.*, "The effects of improper mixing and preferential wetting of active and excipient ingredients on content uniformity in high shear wet granulation," *Powder Technol.*, vol. 278, pp. 266–277, 2015, doi: 10.1016/j.powtec.2015.03.018.

[37] P. Tang and V. M. Puri, "Methods for minimizing segregation: A review," *Part. Sci. Technol.*, vol. 22, no. 4, pp. 321–337, 2004, doi: 10.1080/02726350490501420.

[38] Y. Shi, G. H. Tang, H. F. Lin, P. X. Zhao, and L. H. Cheng, "Dynamics of droplet and liquid layer penetration in three-dimensional porous media: A lattice Boltzmann study," *Phys. Fluids*, vol. 31, no. 4, 2019, doi: 10.1063/1.5091481.

[39] X. Yin, H. Aslannejad, E. T. de Vries, A. Raoof, and S. M. Hassanizadeh, "Droplet Imbibition into Paper Coating Layer: Pore-Network Modeling Simulation," *Transp. Porous Media*, vol. 125, no. 2, pp. 239–258, 2018, doi: 10.1007/s11242-018-1116-0.

[40] M. Denesuk, G. L. Smith, B. J. J. Zelinski, N. J. Kreidl, and D. R. Uhlmann, "Capillary Penetration of Liquid Droplets into Porous Materials," *J. Colloid Interface Sci.*, vol. 158, no. 1, pp. 114–120, 1993, doi: https://doi.org/10.1006/jcis.1993.1235.

[41] Z. Qiao, Z. Wang, C. Zhang, S. Yuan, Y. Zhu, and J. Wang, "PVAm–PIP/PS composite membrane with high performance for CO_2/N_2 separation," *AIChE J.*, vol. 59, no. 4, pp. 215–228, 2012, doi: 10.1002/aic.

Chapter 4. Advanced 3D and 4D Microstructure Study of Single Granule Formation using Synchrotron in-situ X-ray Imaging

The contents of this chapter will be submitted to a peer-reviewed journal for publication.

Contribution of the MSc student

Data analysis and manuscript preparation were performed by Sima Zeinali Danalou. Carter Blocka and Jingsi Yang provided assistance in synchrotron experiments. Ning Zhu and Heather Emady offered technical support in synchrotron-related problems, and experiment design. Ellen Wasan provided guidance on dissolution tests. Lifeng Zhang provided supervision through research and editorial guidance.

Contribution of this chapter to the overall study

This chapter provides a deep understanding of the internal dynamic wet granulation. Synchrotron X-ray was used for the visualization of the process. Pore evolution during the nucleation stage was investigated for the first time. Lastly, the microstructure of the pharmaceutical granule was studied. These findings provided valuable information to understand the process internally and could be used to optimize the wet granulation process for pharmaceutical granules.

4.1 Abstract

Wet granulation is the most common granulation method used in the pharmaceutical and chemical industries. Monitoring the microstructure of the granule in the granulation process could play a decisive role in obtaining high-quality granules. Due to the complex, fast and opaque nature of wet granulation, it cannot be captured by conventional methods (e.g., lab-based X-ray imaging techniques). In this study, synchrotron X-ray imaging was employed for the first time to investigate the internal real-time pore evolution during the granule nucleation process taking place in seconds,

based on the single droplet impact method. Binary mixtures were investigated, consisting of acetaminophen (APAP) as the active pharmaceutical ingredient with lactose monohydrate (LMH) and microcrystalline cellulose (MCC) as excipients. And deionized water was used as a liquid binder. It was found that granules from coarser and more homogenous powders experienced a higher rate of pore evolution during nucleation with a more uniform pore distribution. Dynamic wetting studies showed that the Crater mechanism was found for most binary mixtures with 50 wt. % excipients. The Spreading mechanism occurred for MCC with the greatest droplet diameter increase, and the Tunneling happened for 90 wt. % fine LMH with the highest penetration length. The final granules resulting from the Spreading and Tunneling mechanism showed the highest and lowest porosity, respectively. The tensile strength and dissolution test results showed that the granules with lower porosity and finer pores exhibited higher hardness and a slower dissolution rate.

Keywords: Wet granulation; Nucleation; Porosity; Synchrotron X-ray imaging; Hardness; Dissolution.

4.2 Introduction

Granulation, a particle size enlargement process, has been used to improve final product properties, including hardness, dustiness reduction, and handling. Wet granulation is a common method of granulation in which agglomeration takes place by spraying the liquid binder on the powder particles [1]. It has numerous applications in a wide range of chemical industries, such as pharmaceutical and agriculture. Fundamental steps taking place in wet granulation in the pharmaceutical industry include wetting and nucleation, consolidation and growth, and breakage and attrition. The initial distribution of the droplet inside the powder bed has a pronounced impact on the final granule properties [2]. The nucleation and consolidation stage controls the porosity and voidage inside the final granule, and consequently its hardness and dissolution behavior [3].

An in-depth study of wet granulation steps would be beneficial to choose optimized formulations and operating conditions to obtain granules or tablets with desirable qualities.

The final granule should have sufficient tensile strength and be able to release the components appropriately. The disintegration and dissolution qualify the release profile of the drug release. [4]. And, the dissolution rate importantly determines the active component bioavailability [5]. Tensile strength or hardness is a measure of tablets' strength. Adequate strength avoids deforming tablets during handling and transportation. In addition, tensile strength plays an important role in active component release [4]. The microstructure of final granules affects many properties of the tablet, including disintegration, dissolution, and tensile strength [6]. Tablet porosity, pore size, shape, and tortuosity are all factors influencing the tablet microstructure [7]. The particle size of powders and granulation process conditions (e.g., type and amount of the binder) have a direct impact on final dry granule porosity (Odeku and Itiola, 2003 [4]; Realpe and Velázquez, 2008 [8]). Therefore, monitoring the *in-situ* pore and porosity changes during the granulation process and also the final granule could be helpful in assessing the final granule/tablet quality.

Three granulation mechanisms for wet granulation were developed by Emady et al. [10]: Tunneling, Crater, and Spreading. Tunneling occurs for cohesive powders, where powders aggregate on/in the droplet and tunnel into the powder bed. In contrast, Spreading happens in powders with larger particles, creating the granule on the powder surface. In Crater formation, there is a Crater in the powder bed, and it generally appears at a higher droplet release height. Although the modified Bond number cannot describe the wetting process, it is essential to study the liquid-solid interactions as it quantitatively defines the granule formation mechanism [10]. The larger Bond number indicates the Tunneling mechanism, and the lower number leads to the Spreading or Crater mechanism. Particle size is considered another vital parameter affecting the

wetting process and the final granule formation [9] and is a key variable within the modified Bond number. Several works have previously used the single droplet impact method to study the wet granulation mechanisms [9]–[12]. These studies utilized a high-speed camera to capture the granulation process from the top view of the powder bed. Afterward, final granules were studied based on the morphology and internal structure using a micro-CT system.

Wet granulation is a fast process and powders are typically opaque in nature. Due to the complexity of the granulation system, the evolution of the internal microstructure during granule formation has been unknown due to conventional methods' limitations, such as low spatial and temporal resolution and light scattering [13]. Synchrotron X-ray imaging, as an advanced technique, can be tailored to the sample nature to image the internal structure with high spatial and temporal resolution [14]. Recently, the emerging synchrotron X-ray imaging techniques have been utilized in different applications and pore studies. Zeinali Danalou et al. [15] used synchrotron-based X-ray imaging techniques to investigate the internal porosity of pharmaceutical powder beds and how it affected liquid binder penetration. Kato et al. [16] characterized the pore properties of the washcoat layer in catalysts by using synchrotron X-ray, scanning electron microscopy, and mercury porosimetry in order to evaluate the gas transport. Boudina et al. [17] studied the evolution of the morphometric parameters in microcrystalline cellulose and sugar pellets formed by compaction using X-ray micro-computed tomography. Qie et al. [18] investigated the pore network of Fluid Catalytic Cracking (FCC) particles using X-ray computed tomography combined with a focused ion beam scanning electron microscope (FIB-SEM), for a better understanding of delivering reactants to active sites. These research studies worked on the final product or *in-situ* imaging with low temporal resolutions. Therefore, the objective of this study was to employ synchrotron X-ray micro-computed tomography to track the internal wet granulation process in 3D

53

views and real-time 3D (known as 4D) of pore evolution during the nucleation and granule formation phases in the wet granulation process. Additionally, the final dry granule was studied based on both micro (pore size and distribution and porosity) and macro (hardness and dissolution) scale parameters.

4.3 Materials and Methods

4.3.1 Materials Characterizations

Acetaminophen (APAP) was used as an Active Pharmaceutical Ingredient (API) and purchased by Hebei Jiheng Pharmaceutical. Microcrystalline cellulose (MCC), and lactose monohydrate (LMH), were the excipients used as filler; supplied by FMC BioPolymers, and Foremost Farms, respectively. The liquid binder was deionized (DI) water, one of the most common liquid binders. Similar to our previous work [15], agglomerates were firstly removed from all powders through a 1mm opening size sieve when making binary mixtures. Fine excipients (MCCF and LMHF) were achieved by sieving MCC and LMH through a sieve with an opening size of 38 μm. The formulations of the binary mixtures are shown in Table 4. 1. Bulk binary mixtures of 16 grams were mixed with a Fisherbrand™ Digital Vortex Mixer at 2000 rpm for 10 minutes. Then, for imaging purposes, the powder mixture was loaded into a plastic vial with a height of 2 cm and an inner diameter of 1 cm, with the powder surface leveled. In all experiments, to pour the powder into the vials, a plastic funnel was set up at a height of 1 cm from the top of the vial surface to ensure consistency in sample preparation.

Table 4. 1 Samples formulation. [15]

Sample No.	Sample Name	Excipient Mass Percent (%)		APAP Mass Percent (%)
1	90L-10A	LMH	90	10
2	80L-20A	LMH	80	20
3	50L-50A	LMH	50	50
4	90LF-10A	LMHF	90	10
5	80LF-20A	LMHF	80	20
6	50LF-50A	LMHF	50	50
7	90M-10A	MCC	90	10
8	80M-20A	MCC	80	20
9	50M-50A	MCC	50	50
10	90MF-10A	MCCF	90	10
11	80MF-20A	MCCF	80	20
12	50MF-50A	MCCF	50	50

The powder properties characterized include the median particle size (d_{50}), surface mean diameter (d_s), particle skeletal density (ρ_p), particle bulk density (ρ_{bed}), contact angle with water (θ), modified particle Bond number (Bo_g^*), and aspect ratio (AR). The d_{50} and d_s were obtained by a Malvern 2000 Mastersizer S (Malvern Instruments, UK). The ρ_p was measured with a gas multi-pycnometer (QuantaChrome, Boynton Beach, FL, USA). The ρ_{bed} was measured as the weight per volume in a 100 mL graduated cylinder, after pouring the powder through a plastic funnel at a height of 2 cm and leveling the surface. The particle AR (maximum width/minimum width) was measured based on SEM images presented in our previous work, both fine and coarse particles have similar shapes, so AR was measured just for course ones [15]. The powder-liquid contact angles are taken from our previous work [19]. To describe the powder-liquid interaction that results

in a formed granule, a dimensionless modified particle Bond number was calculated based on the following equation [10]:

$$Bo_g^* = \frac{\gamma \cos\theta}{d_s^2 \rho_{bed} g} \qquad (1)$$

Where γ, θ, d_s, ρ_{bed}, and g are the liquid surface tension, the powder-liquid contact angle, the surface mean particle diameter, the particle bed bulk density, and the gravitational acceleration constant, respectively. The Bo_g^* is the ratio of capillary force and the gravitational force acting on the particle. Thus, this number is useful to study the influence of powder bed packing on wet granulation mechanisms due to liquid bridging. The greater the Bo_g^*, the stronger the liquid-solid interactions and capillary force, resulting in the attachment of powder particles to the liquid droplet [10].

4.3.2 Granule Morphology

After six hours, the dry granule was gently removed from the powder bed by using a spatula. The granule dimensions of maximum diameter (D_{max}), minimum diameter (D_{min}), and height (H_g) were measured with a caliper. After knowing D_{max} or D_{min}, the projected area equivalent diameter (D_a) was calculated based on binarization processing in ImageJ (National Institutes of Health, USA); the projected area is shown as a yellow dashed line in Figure 4. 1. An example of granule size measurements is illustrated in Figure 4. 1. For each composition, three replicates were performed. The morphology of the granule was characterized by the horizontal aspect ratio ($HAR = D_{max}/D_{min}$) , giving information two-dimensional from the top view, and the vertical aspect ratio ($VAR = D_a/H_g$), giving information three-dimensional [9].
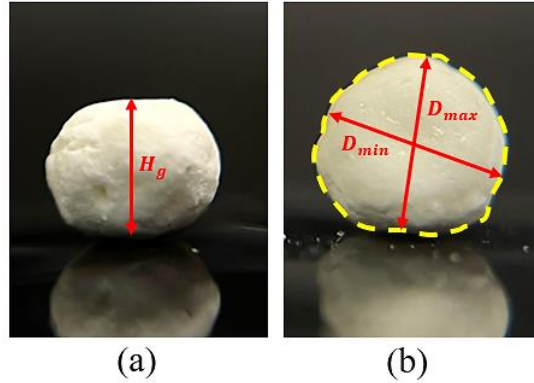
Figure 4.1. Granule morphology measurements: (a) side view; (b) top view.

4.3.3 Granule hardness

The granules all are small with a narrow size range and the shapes vary based on the composition, also they deviate from cylindrical shapes. Thus, to compare granules strength, hardness was measured rather than tensile strength with a texture analyzer (TA.XT plusC from Stable MicroSystems, Godalming, UK). The maximum force (hardness) was calculated by recording the applied force versus distance. The dry granule was placed beneath a 7 mm steel probe and compressed with a trigger force of 0.001 N and a test speed of 0.1 mm/s. The hardness of one sample was measured in three replicates.

4.3.4 In Vitro Dissolution Test

For dissolution tests, 500 mL of buffer simulated gastric fluid (SGF) (pH 1.2) at a speed of 75 rpm (with the use of a stirrer magnet) at 37 ± 1 °C was used. A granule was gently enclosed in a dialysis bag (SpectroPor regenerated cellulose, 10,000-12,000 MWCO) and immersed in the volume. At predetermined times, a 4 mL sample was taken out three times, and then the same amount (12 mL) of fresh SGF was replaced in the flask. To analyze the APAP release profile, and APAP content in the 3 mL sample, the sample was assayed by a UV mini 1240 spectrophotometer (Shimadzu, Kyoto, Japan) and the detection was set at 292 nm.

4.3.5 Synchrotron X-ray CT Setup

The dynamic wet granulation process was captured using the Biomedical Imaging and Therapy Facility (BMIT) 05B1-1 bending magnet beamline at the Canadian Light Source (CLS). A filtered white beam (polychromatic beam) source was utilized for imaging. The projections were captured by an AA-40 beam monitor (Hamamatsu, Japan), LuAG scintillator converting X-rays passed from the sample to visible light, and a DIMAX HS4 camera (PCO AG, Germany). The Field of View (FOV) of the camera was 11 mm x 4 mm (v x h), and the effective pixel size was 5.5 µm [15]. The single drop impact method was conducted to study the dynamic granulation process. A micropipette with a fixed and constant volume of 10 µL was positioned at 2.5 cm from the top surface of the powder bed vial. The sample was placed at 25 m from the X-ray source and 50 cm from the detector. The number of projections per CT was 500 with an exposure time of 1 ms; the interval between two CTs was 1 ms for short processes and approximately 30 s for long processes. The synchrotron radiography setup is shown in Figure 4. 2.
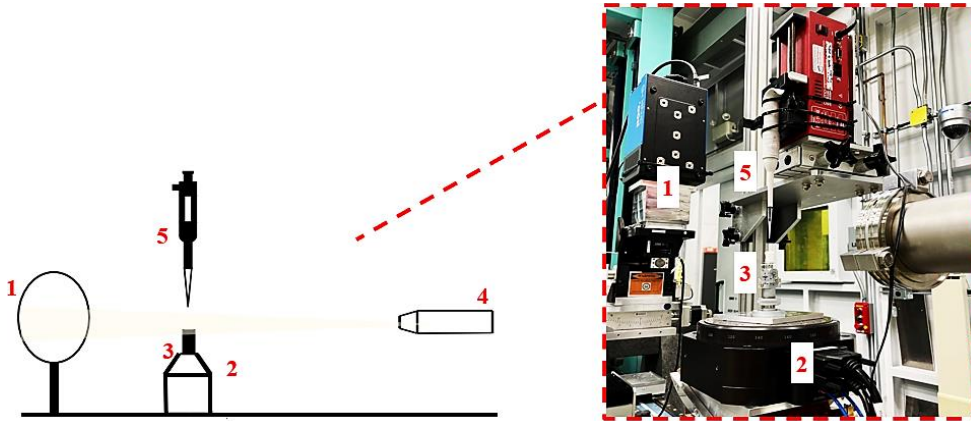

Figure 4. 2. Single drop experimental setup: 1) X-ray detector, 2) Rotary stage, 3) Sample vessel, 4) synchrotron X-ray beam, 5) Micropipettor and Syringe pump.

4.3.6 Image Post-Processing and Analysis

Dark and flat images (no sample and no beam, and with beam and no sample respectively) were captured to normalize the images and perform background correction. UFO-KIT with phase retrieval was employed for tomographic reconstruction [20, 21]. ImageJ (National Institutes of Health, USA) was used for measuring the dimensions, granule physical features, and thresholding. Dragonfly version 2021.1 (Objects Research Systems (ORS) Inc., Canada) was used for 3D rendering and other pore size and porosity measurements.

Different gray values (intensities) are common bases for distinguishing different particles in the images. Particles with higher density better absorb X-ray photons and have a higher attenuation, resulting in lighter gray colors in the CT images [22]. Thus, air with the lowest density appears as black/dark gray. Figure 4. 3 outlines the gray profile for air (which is the same for pores consisting of air inside the granule) and the wet granule. A multistep segmentation process was used to separate a granule from the surrounded powders and segment the pores inside the granule (see Figure 4. 4). Firstly, the Otsu method in Dragonfly, one of the most common methods in image processing, was used to separate light and dark parts, based on the gray value [23]. Then the largest Region of Interest (ROI) was kept and a dilation algorithm was applied to segment the granule. The region out of the granule was segmented by subtracting the total ROI (whole volume including all particles and pores) from the granule. The intensity range of pores was derived from the gray value profile (see Figure 4. 3 b). Based on that range, pores inside the granule were segmented out by subtracting the total pores from the region out of the granule. Next, in order to remove the noise, a 5-pixel radius median filter (erosion) was applied. Lastly, 3D volume rendering was performed.
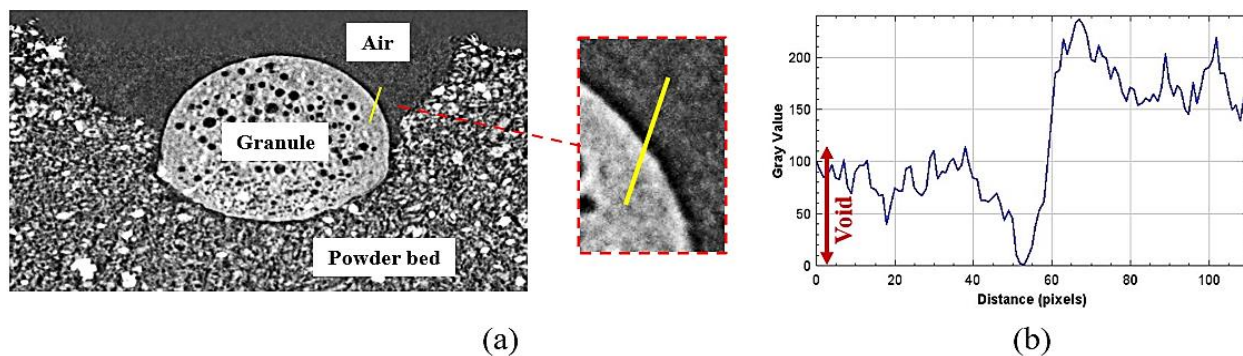
Figure 4. 3. (a) The typical reconstructed slice of 50L-50A; yellow line shows the transition from the air (shown in dark gray) to the granule, (b) The profile of the gray values was plotted of each pixel in the direction of the line.
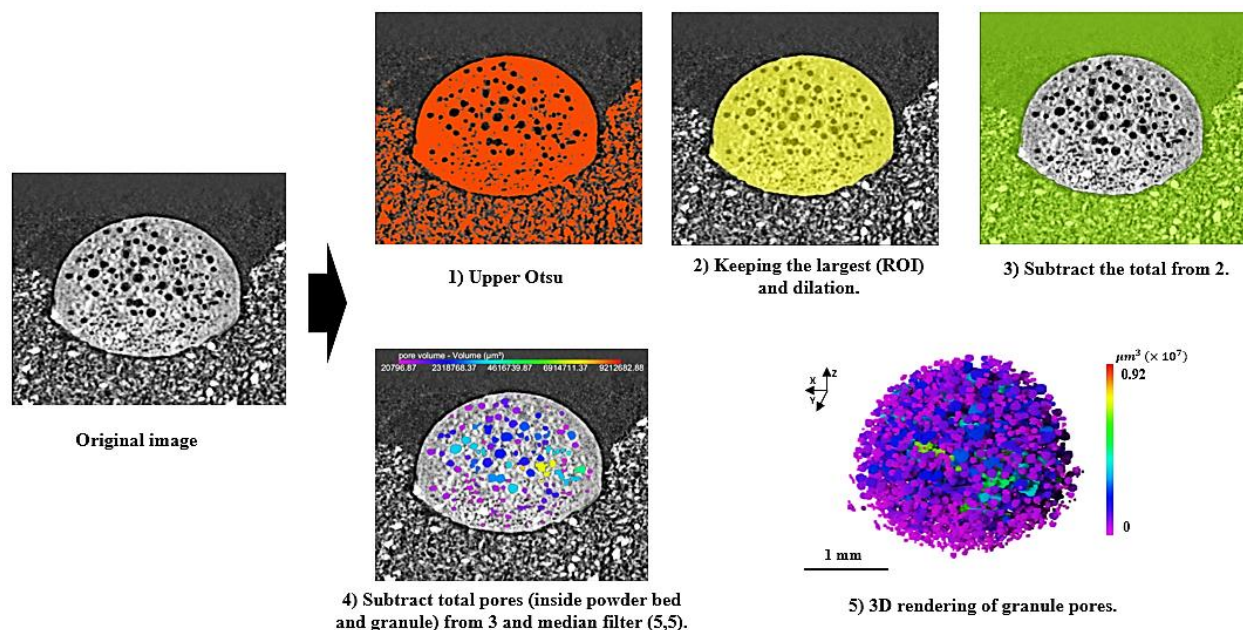
Figure 4.4. Segmentation process of pores in 50L-50A sample

4.4 Results and Discussion

4.4.1 Physical Properties of Pharmaceutical Powders

The physical properties of pharmaceutical powders are shown in Table 4. 2. LMH and APAP had similar median particle sizes of around 50 μm. MCC had the largest median particle size (~110 μm), while LMHF had the smallest (~17 μm). MCC powders made the loosest powder bed, with the lowest bulk density (0.326 g/cm^3). Based on the aspect ratio, both MCC and APAP

60

are rod-shaped. Contact angle quantifies the wettability of the powder with a liquid, where the lower the number represents the higher the wettability. MCC and MCCF were the most wettable powders with the lowest contact angle (45.6 °), and LMHF had the lowest wettability with the highest contact angle (85.3°). The surface tension of deionized water is $72.0\ mN/m$, used in Bo_g^* measurements [24]. Fine powders had the larger Bo_g^* than course ones, as expected [4], LMHF had noticeably the largest modified bond number (2.67E4), while MCC with largest particles had the smallest (2.41E3).

Table 4. 2 Physical properties of pharmaceutical powders.

Powder Component	Median particle size, d_{50} (μm)	Surface mean diameter, d_s (μm)	Particle skeletal density, ρ_p (g/cm³)	Particle bulk density, ρ_{bed} (g/cm3)	Contact angle, θ (°) with water [a]	Modified Bond number, Bo_g^*	Aspect ratio (AR)
Lactose Monohydrate (LMH)	47.9 ± 2.3	21.1± 2.4	1.543± 0.004	0.559 ±0.003	82.7 ± 0.4	3.75E3	1.83
Lactose Monohydrate, fine (LMHF)	16.9 ± 0.5	7.8 ± 0.3	1.542± 0.007	0.370 ±0.007	85.3 ± 2.7	2.67E4	-
Microcrystalline Cellulose (MCC)	110.4 ± 6.6	80.8 ± 5.8	1.555± 0.009	0.326±0.008	45.6 ± 1.2	2.41E3	2.45
Microcrystalline Cellulose, fine (MCCF)	31.8 ± 0.1	24.6± 0.4	1.556± 0.010	0.343±0.009	47.2 ± 6.4	2.40E4	-
Acetaminophen (APAP)	50.9 ± 3.9	17.1± 1.3	1.701± 0.001	0.539±0.002	84.2 ± 0.3	4.71E3	2.59
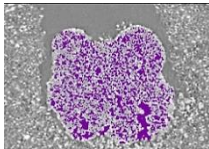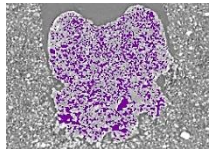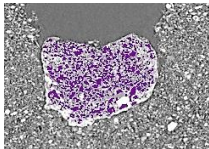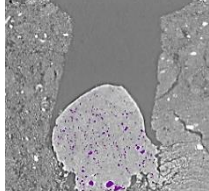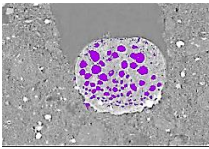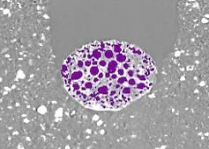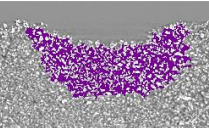
[a][19]
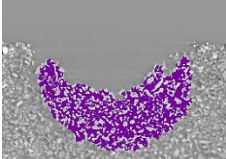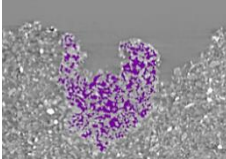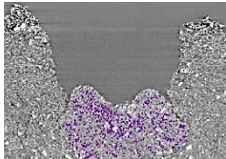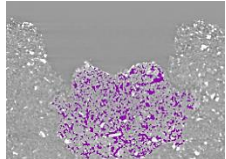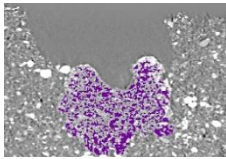
4.4.2 Dynamic Wetting and Granule Formation

4.4.2.1 Granulation Mechanisms

Although granulation mechanisms have been a subject of discussion for some time, due to a lack of advanced tools required to visualize the internals of the powder bed and formed granules, the granulation mechanisms could not be accurately predicted and identified with high certainty. To quantify the granule formation mechanism, the dynamic wetting process is discussed in this section. The penetration time is defined from the moment the droplet contacts the powder bed until it disappears; with the droplet diameter increase (in percentage) measured based on the same timeline. Wetting parameters are presented in Table 4. 3. Wetting followed by nucleation is greatly dependent on the contact angle of the powder with the liquid binder. The liquid droplet penetrates the capillary pores to form the saturated nuclei, and the lower the contact angle and more uniform the pores inside the powder, the faster the resulting wetting and nucleation process [1]. By increasing the number of active components, the penetration time increased for all compositions, as the distribution of the pores became less uniform and the contact angle increased [15]. Regardless of the powder bed porosity, the contact angle played a vital role in wetting, and MCC and MCCF, having a lower contact angle with water (more hydrophilic and higher preferential wetting) experienced much faster penetration, consistent with the literature [1].

Table 4. 3 Wetting parameters. The last column shows the cross-sectional view of granules at the end of wetting, with pores colored in purple.

Composition	Penetration time (s)	Penetration length (mm)	Crater diameter increase (%)	Granulation mechanism	Cross-sectional view (end of penetration)
90L-10A	3.1	2.31	9.1	Transitional (Tunneling / Crater)	
80L-20A	4.2	2.19	8.4	Transitional (Tunneling / Crater)	
50L-50A	870	1.07	3.3	Crater	
90LF-10A	12.2	4.96	2.5	Tunneling	
80LF-20A	720	2.09	5.9	Crater	
50LF-50A	1110	1.24	6.2	Crater	
90M-10A	0.03	0.51	31.1	Spreading	

80M-20A	0.16	0.90	24.6	Spreading	
50M-50A	0.30	1.25	15.2	Transitional (Spreading/ Tunneling)	
90MF-10A	0.25	1.9	2.8	Transitional (Tunneling/ Crater)	
80MF-20A	0.30	2.15	4.8	Transitional (Tunneling/ Crater)	
50MF-50A	0.39	1.50	3.8	Crater	

Almost all of the fine compositions had a longer penetration length than those from the coarse ones, especially for 90LF-10A with a Tunneling mechanism (4.96 mm), and the granules were formed at the powder surface for Spreading mechanisms (90M-10A and 80M-20A), which is in line with the Bond numbers for pure MCC and LMHF. In the Tunneling mechanism, powders aggregate inside the droplet and then tunnel into the powder bed. According to the literature, the penetration distance of the liquid from the same binder is dependent on the contact angle and radius of pores [25, [6]. As shown in Figure 4. 5, the 90LF-10A powder bed had excessive fine pores, resulting in capillary fluid flow thus drawing the binder droplet into the powder bed. MCCF

had the second-highest Bond number (2.40E4), but based on the image sequences and wetting parameters, 90% and 80% of MCCF are in transition between the Crater and Tunneling mechanisms. The increase of crater diameter is another important factor in determining the process; those with an increase of more than 25% (90M-10A and 80M-20A) are in the spreading category [11]; other mechanisms had varying diameter increase ranges. For instance, 50M-50A had a smaller diameter increase and longer penetration length, so it would be in a hybrid mechanism between Spreading and Tunneling. Generally, the Tunneling/Crater mechanism resulted in a lower diameter increase than that from the spreading/Tunneling mechanism, but larger than tunneling; furthermore, the Tunneling/Crater mechanism had a larger diameter increase than the Crater mechanism. The Crater mechanism was observed for 50% of LMH, LMHF, and MCCF, where the powder bed did not have uniform pore distribution [15] preventing the droplet from penetrating; as a result after the first impact and crater formation, the droplet remained there and the granule was formed by immersing the nearby powders inside the granule. So, for the compositions with Crater mechanisms, penetration length is shorter and the penetration time is longer compared with higher fractions of the same excipients. To better illustrate the mechanisms, Figure 4. 6 shows the time sequence of cross-sectional views from the 3D volume of different granulation mechanisms.
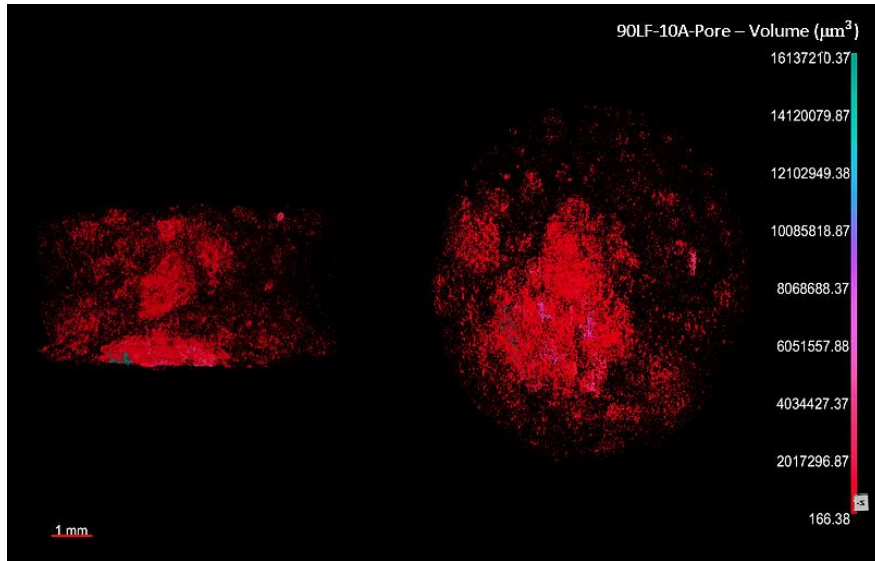
Figure 4. 5. Pores volume after omitting the first large connected pore for 90LF-10A. left: YZ; right XY view.
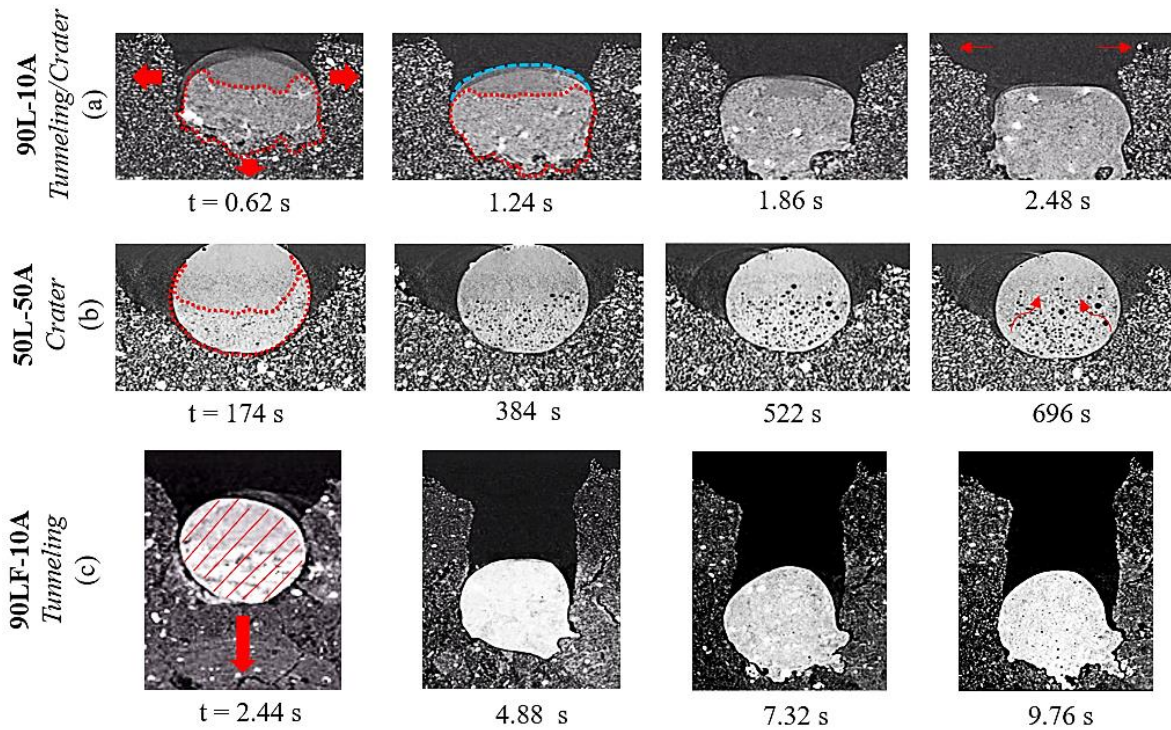
Figure 4. 6. Image sequence of single droplet granulation. (a) Tunneling/Crater mechanism; (b) Crater mechanism; (c) Tunneling mechanism. The blue dashed line shows the droplet, and the red dashed line shows the granule.

4.4.2.2 Granule Formation and Pore Evolution

The first stage in wet granulation is nucleation, where the droplet contacts the powder bed and penetrates into the bed to form a granule. Based on the steps discussed in section 2.6, pores were segmented out from the granule inside the powder bed in Dragonfly. For studying the granule formation and pore evolution process, 50 wt.% and 90 wt.% of excipients were investigated for the internal study of single drop granulation. For brevity, six-time intervals, from the moment the droplet disappears, were selected for this purpose. LMH partially dissolves into the water, resulting in longer wetting and consolidation than MCC mixtures [15].

Figure 4. 7 shows the changes in the porosities and the mean pore volumes of the granules over time. Most coarse compositions (with the same fraction) had a higher pore (mean pore volume) evolution rate than those of the fine counterparts. Additionally, in the same powders, in most of the 90% fractions, the pores enlarged faster than in the 50% fractions. According to the previous study [15], generally coarser and more homogeneous (90% excipient) powders have more uniform particles and pore distribution along axes in the powder bed, in which the wetting and nucleation will take place smoothly and pore size enlargement would be faster and easier. Also, the granulation mechanism showed an important impact on the pore evolution; if the granule was closer to the bed surface and no droplet was trapped inside, the evaporation of the binder would also play an important role in accelerating the pore evolution. For example, 90M-10A, with a Spreading mechanism, had the fastest pore evolution and the highest porosity (reaching 40%). In contrast, 90LF-10A, with the tunneling mechanism (having the granule deep inside the powder bed, as can be seen in Table 4. 3) experienced the slowest pore evolution, with the lowest porosity at the end (5%).
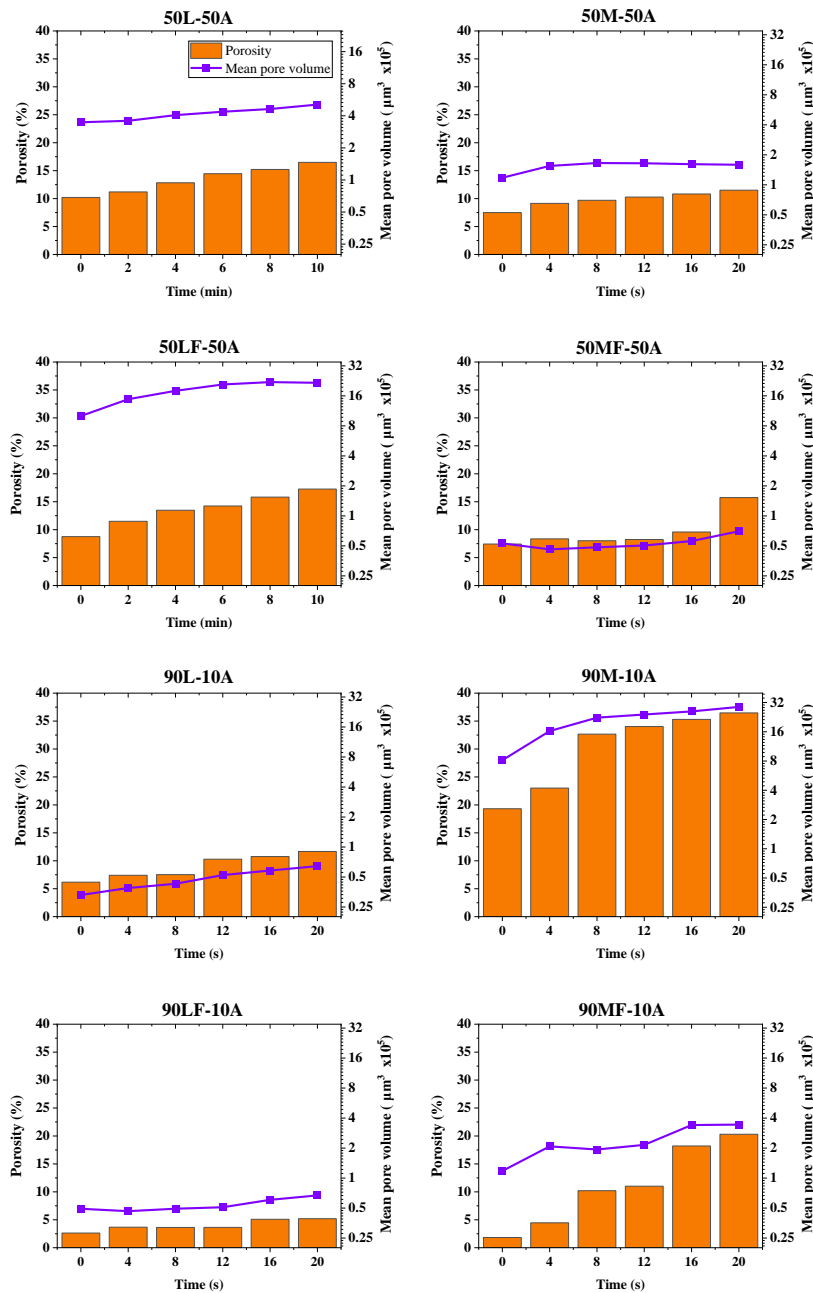
Figure 4. 7. Pore evolution with time. For 50L-50A and 50LF-50A, time intervals were selected as 2 minutes, and for the remaining compositions, pores were evaluated every 4 seconds. (Bar chart: Porosity, Line: Mean pore volume)

4.4.2.2.1 3D Color Mapping and Pore Distribution

For a better understanding of the granule rheology and pore sizes and mapping, 3D volume rendering was applied with results shown in Figure 4. 8. For the 50L-50A and 50LF-50A samples, due to the solid layer on the droplet during wetting and dissolution of excipients in the droplet, there are air bubbles trapped in the granule, especially in the case of 50LF-50A with a larger pore volume. Among all samples, 90L-10A and 90LF-10A had the most uniform small pore distributions ($V\ pore \cong 0.87 \times 10^7\,\mu m^3$) (as seen in purple). 90M-10A had significantly larger pores ($V\ pore = 880 \times 10^7\,\mu m^3$), for practically all regions of the granule, also the granule experienced size enlargement via a layer-by-layer mechanism as well [27]. Additionally, 90MF-10A had large pores ($V\ pore = 103 \times 10^7\,\mu m^3$), but were mostly located at the upper parts of the granule.

Other than the porosity, pore alignment has significant effects on the final granule properties such as drug release kinetics [28]. Figure 4. 9 illustrates the distribution of the pores from the top to the bottom of the granule, at the fifth time point (at 8 min or 16 s, depending on the compositions), demonstrating how much of the area of the horizontal plane from the top to the bottom of the granule is covered by pores (in percentage). Thus, higher porosity at the fifth time (see Figure 4. 7) would result in a higher percentage of pores in Figure 4.9. Uniform pores and ingredient distribution inside the granule are key factors in ensuring targeted hardness and dissolution of pharmaceutical components [29]. As can be seen in Figure 4. 9, the pore distribution in most LMH and LMHF compositions (especially 50L-50A) followed a symmetrical pattern (shown with a dashed line). However, there are a lot of fluctuations in 90LF-10A, which would be one of the reasons for having low hardness. For 90M-10A, pores are present in more than 30% of the

69

area at a large portion of the central volume. There are sharp changes in pore volume in 50LF-50A, 50MF-50A, and 90MF-10A, which will result in the fragility of the dry granule.
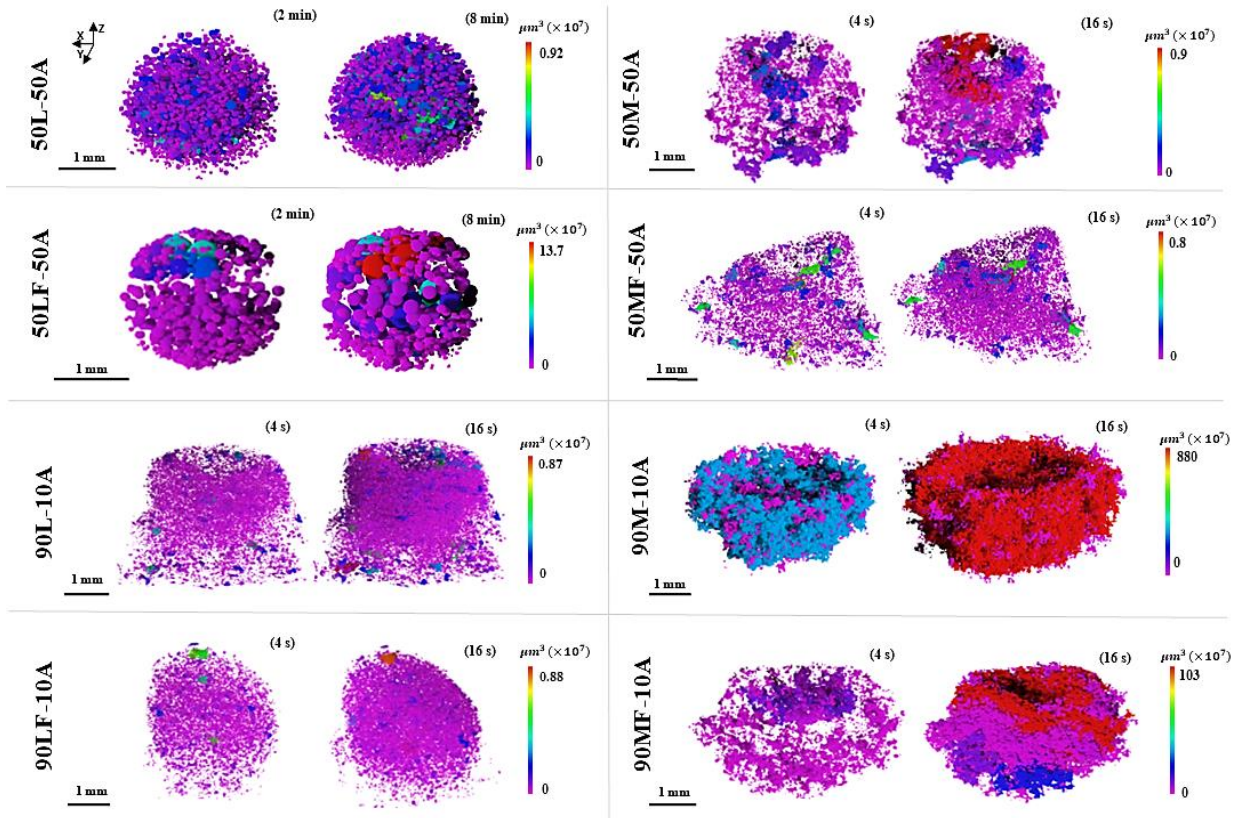
Figure 4. 8. 3D pores volume rendering over time. The left and right images for each composition are the second and fifth time points (among six). The maximum value of the color legend (maximum pore volume) varies based on the composition.
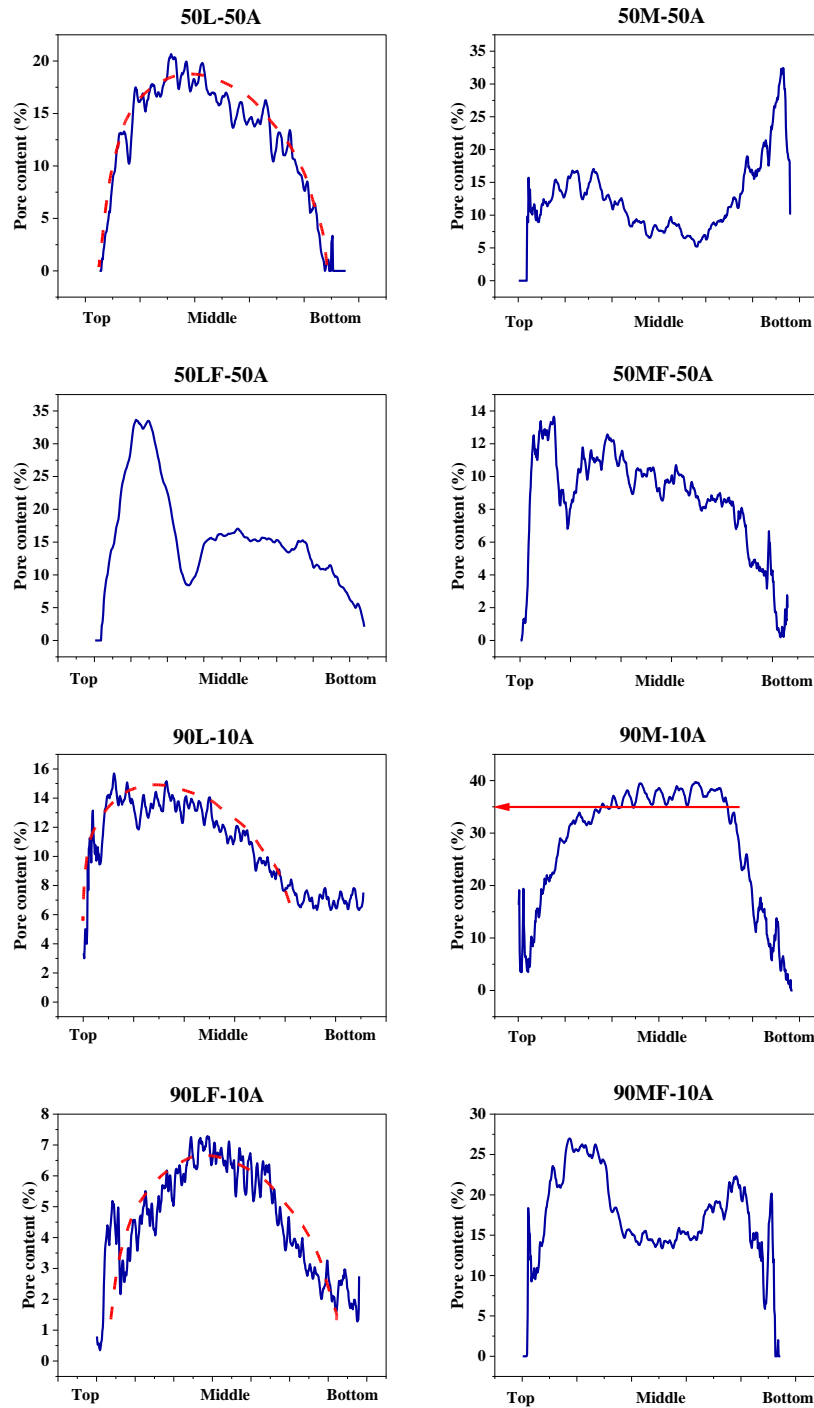
Figure 4. 9. Area percentage of pores along the z-direction (top to bottom of the granule). Dashed red lines show asymmetric pore distribution.

4.4.3 Dry Granule

4.4.3.1 Dry Granule Internal Structure

The same method discussed in the previous sections was applied to dry granules to segment out the pores. The porosity was calculated by dividing the total volume of pores by the total granule volume. Pore size analysis is necessary to understand the microstructure and its linkage to the mechanical properties of the final granules [30]. The porosity values of dry granules are shown in Figure 4. 10 a. For most of the binary mixtures, the overall trend of porosity changes in the granules (upward or downward) is the same as the trends for the powder bed porosities seen in our previous work [15]. LMH, particularly LMHF, acted as the solid binder, effectively binding the particles and producing final granules with lower porosities. [31]. As LMH and APAP had similar particle sizes, increasing the APAP content did not noticeably change the granule porosity. The granule formed by the Tunneling mechanism (90LF-10A) had the smallest porosity among all compositions [12]. As the droplet could not spread further to make the bridges to the powder particles, pores did not develop. With increasing APAP content, the granulation mechanism moved into the Crater mechanism and the porosity increased. The granules formed by MCC (with spreading or Spreading/Tunneling mechanism) had the greatest porosity values (37-52%), as expected from the nucleation steps (see Figure 4. 6). The mean pore volume of different compositions is shown in Figure 4. 10 b. Among LMH compositions, 80L-20A had the lowest mean pore volume. Among all compositions, 90LF-10A had the lowest mean pore volume, because of its granulation mechanism (Tunneling), as the bridges between liquid and solid did not develop properly and there was no significant pore evolution. In contrast, 90M-10A had the highest mean pore volume. Among MCCF compositions, when increasing the APAP concentration, the overall particle size increased, and the mean pore volume increased as well [5, 12].
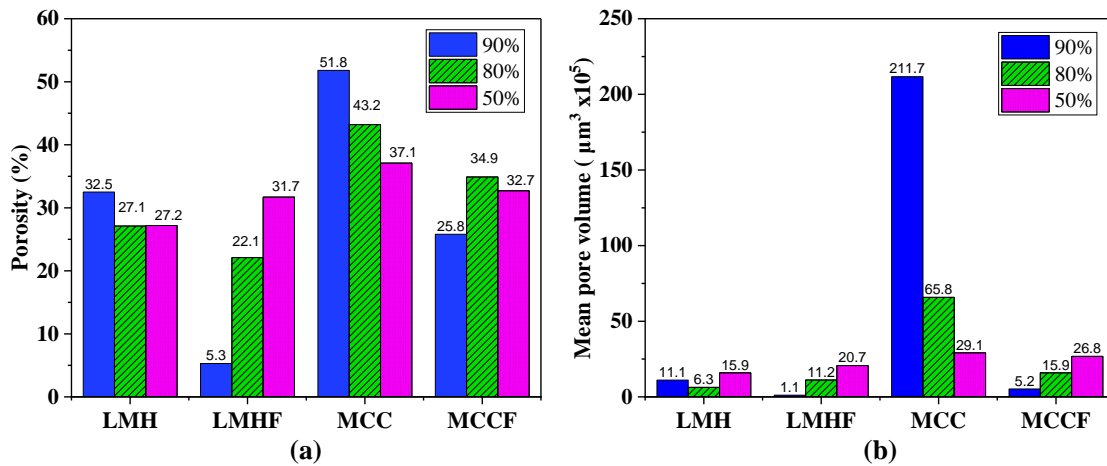
Figure 4. 10. Pore information in the final granules: (a) porosity; (b) mean pore volume. 90%, 80%, and 50% are the mass percent of the excipient mixtures with APAP.

4.4.3.2 Dry Granule Morphology and Physical Tests

The particle size and morphology are shown in Table 4. 4. Generally, MCC and MCCF formed flatter granules with higher VAR, particularly at higher fractions of the excipient with the Spreading mechanism [12]. As seen, 90LF-10A with the Tunneling mechanism had the lowest VAR value. The granules formed from the Crater mechanism (the ones with a longer granulation process) were the smallest in size with a more roundish shape from the top view (HAR =1-1.1), consistent with the literature [10, 32], meaning that they had similar D_{max} and D_{min}. This can be explained by the formation mechanism. As the droplet did not spread and just the powders in the crater were immersed into the granule, the granule would be formed in the shape of a spherical droplet. In addition, for most of the cases, when increasing the APAP content from 10% to 50%, both HAR and VAR decreased.

The results for the hardness of the final granules are also provided in Table 4. 4. As the granules formed from 90M-10A and 80M-20A were very fragile, their hardness could not be measured.

73

The hardness or tensile strength of granules or tablets depends on parameters such as particle size, porosity, pore size, pore shape, and pore distribution [33– 36]. All LMH and LMHF compositions had higher hardness than those of MCC and MCCF, as lactose monohydrate acted as a binder and the cohesion effect prevented the granule from breaking [37]. According to [34], there is an increased breaking force of the tablets by decreasing the volume of large pores and shifting to the pores with smaller pore diameters. 80% of LMH and LMHF had the largest hardness due to quite a small particle size and cohesion effect, and they had suitable porosity and relatively small mean pore volume, notably in the case of 80L-20A with a mean pore volume of 6.3×10^5 μm^3. LMH and APAP, have similar particle sizes, resulting in higher hardness. 50LF-50A had higher porosity, mean pore volume, and non-uniform pore distribution, resulting in lower hardness among LMH and LMHF compositions. For 90LF-10A, due to its Tunneling granulation mechanism, the particle-droplet bridges did not form, and despite low porosity and mean pore volume, the hardness was found to be low. MCCF and especially MCC compositions had elongated and large pores due to their large particle size and shape (rod-shaped). In addition, there is no uniform pore distribution inside the granule (see Figs. 6 and 7). Generally, by increasing the granule porosity and pore size, the tensile strength decreases [35]. The porosity and mean pore volume of the MCC composition were significantly higher, leading in the lowest strength. Although 90MF-10A had lower porosity and mean pore volume, it did not have uniform pore distribution and so had a low high hardness; however, 50MF-50A had slightly greater strength because to its more uniform pore distribution (see Figure 4. 7).

74

Table 4. 4 Size, shape, and hardness of the final granules. The top view of granules is presented in the last column.

Composition	D_{max} (mm)	D_{min} (mm)	D_a (mm)	H_g (mm)	HAR (D_{max}/D_{min})	VAR (D_a/H_g)	Hardness (N)	Top view- real image
90L-10A	5.43 ± 0.07	4.49 ± 0.11	4.96 ± 0.03	3.75 ± 0.04	1.21	1.32	3.68 ± 0.45	
80L-20A	4.65 ± 0.1	3.95 ± 0.37	3.90 ± 0.11	4.55 ± 0.02	1.18	0.86	12.45 ± 0.31	
50L-50A	3.14 ± 0.33	2.89 ± 0.04	2.78 ± 0.06	2.50 ± 0.28	1.09	1.11	3.06 ± 0.41	
90LF-10A	4.03 ± 0.1	3.38 ± 0.13	3.85 ± 0.09	4.38 ± 0.24	1.19	0.88	2.68 ± 0.33	
80LF-20A	2.80 ± 0.03	2.76 ± 0.01	2.90 ± 0.07	2.47 ± 0.09	1.02	1.17	6.82 ± 0.49	
50LF-50A	2.68 ± 0.06	2.65 ± 0.07	2.64 ± 0.07	1.75 ± 0.14	1.01	1.51	1.58 ± 0.45	
90M-10A	5.35 ± 0.15	4.38 ± 0.09	4.79 ± 0.09	2.17 ± 0.12	1.22	2.21	N/A (Broken)	
80M-20A	4.78 ± 0.49	3.84 ± 3.51	4.46 ± 0.17	2.60 ± 0.13	1.25	1.72	N/A (Broken)	
50M-50A	4.10 ± 0.18	3.51 ± 0.11	3.99 ± 0.13	2.96 ± 0.05	1.17	1.35	0.08 ± 0.06	
90MF-10A	4.55 ± 0.05	4.00 ± 0.10	4.48 ± 0.08	2.60 ± 0.10	1.14	1.72	0.09 ± 0.01	
80MF-20A	4.44 ± 0.12	3.73 ± 0.12	3.92 ± 0.11	2.60 ± 0.10	1.19	1.51	0.07 ± 0.05	
50MF-50A	2.75 ± 0.02	2.60 ± 0.10	2.72 ± 0.07	1.66 ± 0.05	1.06	1.64	1.37 ± 0.37	

The granules from 80 wt.% of LMH, LMHF, MCC, and MCCF for the dissolution test, as they had relatively larger hardness compared to other mixtures. The 80M-20A sample was very fragile due to higher porosity and larger mean pore volume. Once this sample was put in the dialysis bag, it was immediately dissolved. Dissolution profiles for the remaining compositions are shown in Fig 11. Granule microstructure and porosity have a pronounced effect on deformation and dissolution behavior [5]. 80MF-20A, with the high porosity and low hardness, had a much faster dissolution rate, reaching 100% of drug release in 20 minutes. Although 80L-20A had higher hardness, 80LF-20A had lower porosity, and due to its Crater formation mechanism and smaller granule size, it would have higher tensile strength [38]. So, with a slower dissolution profile, it slowly disintegrated and completely dissolved at 55 minutes, which was slightly longer than the 80L-20A sample.
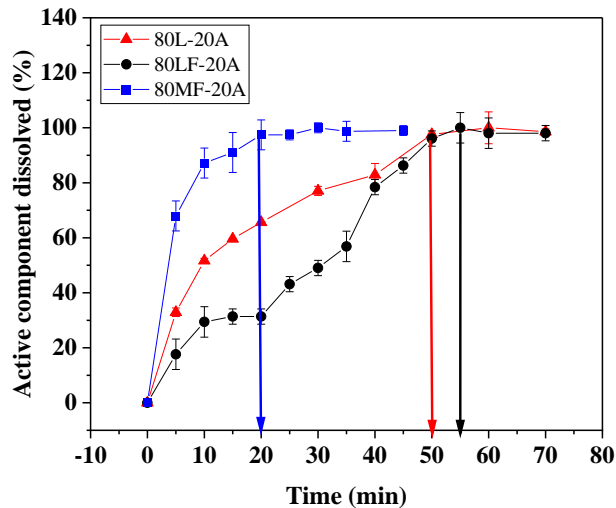
Figure 4. 11 . Dissolution profile. Arrows show the time that complete dissolution of the active component was achieved.

4.5 Conclusions

In this work, the dynamic wet granulation process and the resultant granules were studied using synchrotron-based X-ray CT techniques based on the single droplet impact method. The liquid binder was deionized water, and powders were binary mixtures of APAP as the API LMH and MCC as two common excipients. The findings of this work are as follows:

- The pore size and arrangement inside the powder bed, directly impact on wet granulation process.

- The coarser powders had faster pore evolution with larger pores. Also, at higher excipient fractions, pores are distributed more uniformly. In most LMH and LMHF compositions, pores followed a symmetrical distribution from the top to the bottom of the granule.

- Penetration time became longer by increasing the APAP content. Particle size is a predominant factor influencing the granulation mechanisms. In 90LF-10A, with small particle size, the Tunneling mechanism occurred, with a long penetration length. In contrast, for coarse powders, the Spreading mechanism happened. Most of the 50% of excipients experienced the Crater mechanism (with longer penetration time), due to non-uniform pore and particle distribution in the powder bed. Other compositions had hybrid and transition mechanisms.

- The granules formed through the Tunneling mechanism had the lowest porosity and mean pore volume, and the ones via Spreading had the largest porosity and mean pore volume. Generally, by increasing the amount of powder with a larger particle size, the porosity and mean pore volume increased as well.

- All LMH and LMHF samples had higher hardness, as they bind the particles very well. 80% of LMH and LMHF had the highest hardness due to the suitable porosity and small mean pore volume. Generally, by increasing the porosity, the hardness and the dissolution rate decreased.

This study demonstrated the potential of using the Synchrotron X-ray imaging technique to monitor the wet granulation process *in-situ* and, for the first time, provided information on pore evolution during the nucleation phase. This is necessary to obtain granules with suitable porosity and a relatively short process time. The new knowledge obtained will enable appropriate wet granulation conditions and powder selection in the chemical, pharmaceutical, food science, and agricultural industry.

4.6 Acknowledgments

4.7 References

[1]   S. M. Iveson, J. D. Litster, K. Hapgood, B. J. Ennis, "Nucleation, growth and breakage phenomena in agitated wet granulation processes: a review" , *Powder Technol.*, vol. 117, no. 1, pp. 3–39, 2001, doi: https://doi.org/10.1016/S0032-5910(01)00313-8.

[2]   D. M. Parikh, Ed., Handbook of pharmaceutical granulation technology. Taylor & Francis Group, 2005.

[3]   A. Moradikouchi, A. Sparén, S. Folestad, J. Stake, H. Rodilla, "Terahertz frequency domain sensing for fast porosity measurement of pharmaceutical tablets" , *Int. J. Pharm.*, vol. 618, no. February, pp. 4–9, 2022, doi: 10.1016/j.ijpharm.2022.121579.

[4]   O. A. Odeku, O. A. Itiola, "Evaluation of the effects of khaya gum on the mechanical and release properties of paracetamol tablets" , *Drug Dev. Ind. Pharm.*, vol. 29, no. 3, pp. 311–

320, 2003, doi: 10.1081/DDC-120018205.

[5]   M. A. Ansari, F. Stepanek, "The effect of granule microstructure on dissolution rate", *Powder Technol.*, vol. 181, no. 2, pp. 104–114, 2008, doi: 10.1016/j.powtec.2006.12.012.

[6]   C. C. Sun, "Microstructure of Tablet—Pharmaceutical Significance, Assessment, and Engineering", *Pharm. Res.*, vol. 34, no. 5, pp. 918–928, 2017, doi: 10.1007/s11095-016-1989-y.

[7]   D. Markl *et al.*, "Resolving the rapid water absorption of porous functionalised calcium carbonate powder compacts by terahertz pulsed imaging", *Chem. Eng. Res. Des.*, vol. 132, pp. 1082–1090, 2018, doi: 10.1016/j.cherd.2017.12.048.

[8]   A. Realpem C. Velázquez, "Growth kinetics and mechanism of wet granulation in a laboratory-scale high shear mixer: Effect of initial polydispersity of particle size", *Chem. Eng. Sci.*, vol. 63, no. 6, pp. 1602–1611, 2008, doi: 10.1016/j.ces.2007.11.018.

[9]   H. N. Emady, D. Kayrak-Talay, W. C. Schwerin, J. D. Litster, "Granule formation mechanisms and morphology from single drop impact on powder beds", *Powder Technol.*, vol. 212, no. 1, pp. 69–79, 2011, doi: 10.1016/j.powtec.2011.04.030.

[10]   H. N. Emady, D. Kayrak-Talay, J. D. Litster, "A Regime Map for Granule Formation by Drop Impact on Powder Beds", *AIChE J.*, vol. 59, 2013, doi: 10.1002/aic.

[11]   T. Gao *et al.*, "Powder bed packing and API content homogeneity of granules in single drop granule formation", *Powder Technol.*, vol. 366, pp. 12–21, 2020, doi: 10.1016/j.powtec.2020.02.039.

[12]   T. Gao *et al.*, Granule formation and structure from single drop impact on heterogeneous powder bed*s*, *Int. J. Pharm.* vol. 552, no. 1–2. 2018.

[13]   M. Gonçalves *et al.*, "Droplet evaporation on porous fabric materials", *Sci. Rep.*, vol. 12, no. 1, pp. 1–11, 2022, doi: 10.1038/s41598-022-04877-w.

[14]   C. Karunakaran *et al.*, "Factors influencing real time internal structural visualization and dynamic process monitoring in plants using synchrotron-based phase contrast X-ray imaging", *Sci. Rep.*, vol. 5, no. 1, p. 12119, 2015, doi: 10.1038/srep12119.

[15]   S. Zeinali Danalou, X. F. Ding, N. Zhu, H. N. Emady, Z. Lifeng, "4D Study of Liquid

Binder Penetration Dynamics in Pharmaceutical Powders using Synchrotron X-ray Micro Computed Tofile:///C:/Users/10/Desktop/paper2/Chemi3.pdfmography" , *Int. J. Pharm.*, 2022. [Submitted]

[16] S. Kato *et al.*, "Characterization of secondary pores in washcoat layers and their effect on effective gas transport properties" , *Chem. Eng. J.*, vol. 324, pp. 370–379, 2017, doi: 10.1016/j.cej.2017.05.055.

[17] I. Boudina, E. Rondet, S. Nezamabadi, T. Sharkawi, "Insight into tableted pellets by combining X-ray micro-computed tomography and experimental compaction" , *Powder Technol.*, vol. 397, p. 117083, 2022, doi: 10.1016/j.powtec.2021.117083.

[18] Z. Qie *et al.*, "Multiscale investigation of pore network heterogeneity and permeability of Fluid Catalytic Cracking (FCC) particles" , *Chem. Eng. J.*, vol. 440, no. March, p. 135843, 2022, doi: 10.1016/j.cej.2022.135843.

[19] C. Li, Y. Zhang, N. Zhu, H. N. Emady, L. Zhang, "Experimental investigation of wet pharmaceutical granulation using in-situ synchrotron X-ray imaging" , *Powder Technol.*, vol. 378, pp. 65–75, 2021, doi: 10.1016/j.powtec.2020.09.063.

[20] T. Faragó *et al.*, " Tofu : A fast, versatile and user-friendly image processing toolkit for computed tomography" , *J. Synchrotron Radiat.*, vol. 29, no. 3, pp. 916–927, 2022, doi: 10.1107/s160057752200282x.

[21] M. Vogelgesang *et al.*, "Real-time image-content-based beamline control for smart 4D X-ray imaging" , *J. Synchrotron Radiat.*, vol. 23, pp. 1254–1263, 2016, doi: 10.1107/S1600577516010195.

[22] W. A. Kalender, *Computed tomography fundamentals, system technology, Image Quality, Applications*, vol. 4, no. 1. 2011.

[23] L. Jianzhuang, L. Wenqing, T. Yupeng, "Automatic thresholding of gray-level pictures using two-dimension Otsu method" , *in* China*., 1991 International Conference on Circuits and Systems*, 1991, pp. 325–327 vol.1, doi: 10.1109/CICCAS.1991.184351.

[24] X. Y. Hua, M. J. Rosen, "Dynamic surface tension of aqueous surfactant solutions. I. Basic paremeters" , *J. Colloid Interface Sci.*, vol. 124, no. 2, pp. 652–659, 1988, doi:

10.1016/0021-9797(88)90203-2.

[25]　L. Forny, A. Marabi, S. Palzer, "Wetting, disintegration and dissolution of agglomerated water soluble powders" , *Powder Technol.*, vol. 206, no. 1–2, pp. 72–78, 2011, doi: 10.1016/j.powtec.2010.07.022.

[26]　S. Ahmadian, S. Moradian, A. Sharif, "Prediction of Time of Capillary Rise in Porous Media Using Artificial Neural Network (ANN)" , *Iran. J. Chem. Chem. Eng.(IJCCE)*, vol. 26, no. 1, pp. 71–83, 2007.

[27]　T. Lee, F. Bin Hsu, "A cross-performance relationship between carr's index and dissolution rate constant: The study of acetaminophen batches" , *Drug Dev. Ind. Pharm.*, vol. 33, no. 11, pp. 1273–1284, 2007, doi: 10.1080/03639040701542390.

[28]　B. Zhang, A. Gleadall, P. Belton, T. Mcdonagh, R. Bibb, S. Qi, "New insights into the effects of porosity, pore length, pore shape and pore alignment on drug release from extrusionbased additive manufactured pharmaceuticals" , *Addit. Manuf.*, vol. 46, no. February, p. 102196, 2021, doi: 10.1016/j.addma.2021.102196.

[29]　L. Wagner-Hattler *et al.*, "Study of drug particle distributions within mini-tablets using synchrotron X-ray microtomography and superpixel image clustering" , *Int. J. Pharm.*, vol. 573, no. October 2019, p. 118827, 2020, doi: 10.1016/j.ijpharm.2019.118827.

[30]　A. K. Schomberg, A. Diener, I. Wünsch, J. H. Finke, A. Kwade, "The use of X-ray microtomography to investigate the microstructure of pharmaceutical tablets: Potentials and comparison to common physical methods" , *Int. J. Pharm. X*, vol. 3, p. 100090, 2021, doi: 10.1016/j.ijpx.2021.100090.

[31]　G. M. Laudone, G. P. Matthews, P. A. C. Gane, C. J. Ridgway, J. Schoelkopf, "Estimation of the effective particle sizes within a paper coating layer using a void network model" , *Chem. Eng. Sci.*, vol. 60, no. 23, pp. 6795–6802, 2005, doi: 10.1016/j.ces.2005.06.002.

[32]　H. Ma, G. P. Andrews, D. S. Jones, G. M. Walker, "Low shear granulation of pharmaceutical powders: Effect of formulation on granulation and tablet properties" , *Chem. Eng. J.*, vol. 164, no. 2, pp. 442–448, 2010, doi: https://doi.org/10.1016/j.cej.2009.11.014.

[33]　J. Nordström, A. S. Persson, L. Lazorova, G. Frenning, G. Alderborn, "The degree of

compression of spherical granular solids controls the evolution of microstructure and bond probability during compaction" , *Int. J. Pharm.*, vol. 442, no. 1–2, pp. 3–12, 2013, doi: 10.1016/j.ijpharm.2012.08.011.

[34] A. M. Juppo, "Relationship between breaking force and pore structure of lactose, glucose and mannitol tablets" , *Int. J. Pharm.*, vol. 127, no. 1, pp. 95–102, 1996, doi: 10.1016/0378-5173(95)04203-2.

[35] M. P. J. Schöpfer, S. Abe, C. Childs, J. J. Walsh, "The impact of porosity and crack density on the elasticity, strength and friction of cohesive granular materials: Insights from DEM modelling" , *Int. J. Rock Mech. Min. Sci.*, vol. 46, no. 2, pp. 250–261, 2009, doi: 10.1016/j.ijrmms.2008.03.009.

[36] S. Grote, P. Kleinebudde, "Roll Compaction/Dry Granulation of Dibasic Calcium Phosphate Anhydrous—Does the Morphology of the Raw Material Influence the Tabletability of Dry Granules?" , *J. Pharm. Sci.*, vol. 107, no. 4, pp. 1104–1111, 2018, doi: 10.1016/j.xphs.2017.12.003.

[37] M. B. MacKaplow, L. A. Rosen, J. N. Michaels, "Effect of primary particle size on granule growth and endpoint determination in high-shear wet granulation" , *Powder Technol.*, vol. 108, no. 1, pp. 32–45, 2000, doi: 10.1016/S0032-5910(99)00203-X.

[38] G. M. Walker, C. R. Holland, M. M. N. Ahmad, D. Q. M. Craig, "Influence of process parameters on fluidised hot-melt granulation and tablet pressing of pharmaceutical powders" , *Chem. Eng. Sci.*, vol. 60, no. 14, pp. 3867–3877, 2005, doi: 10.1016/j.ces.2005.02.007.

Chapter 5. Conclusions and Recommendations

5.1 Conclusions

An advanced synchrotron-based X-ray imaging technique was used to visualize the internal pore structures (both 2D and 3D) of pharmaceutical powders and dynamic binder droplet penetration (real-time 3D or 4D). The research results revealed a close correlation between powder bed packing properties and dynamic wetting and nucleation processes of wet granulation and lastly the properties of the final granules.

In the first phase, for powder binary mixtures of lactose monohydrate (LMH) and microcrystalline cellulose (MCC) with acetaminophen (APAP), the porosity, mixing quality, particles, and pores distribution along Z axes were investigated in the static powder bed. It was found that powder beds with higher homogeneity and larger particles had a more uniform pore distribution. It was also discovered that porosity and arrangements of pores depending on particle size played the most crucial role in the properties mentioned above. Lower porosities were observed in LMH mixes with decreased size ratios between X and Y axes. And for the particles with different sizes, the porosity increased by increasing one of the components and the existence of additional void spaces.

Uniform pore distribution along the path of the droplet penetration is responsible for faster penetration time and shorter penetration length. Furthermore, larger porosity resulted in faster penetration. During the penetration process, there was a competitive tendency between the droplet spreading and imbibition; as for fine microcrystalline cellulose, the imbibition rate with isopropanol was constant whereas the droplet width changed more considerably.

For the first time, the internal pore evolution during the nucleation and granule formation in pharmaceutical powders with water was studied. The coarser particles evolved faster and had

larger pores, mainly due to uniform pore distribution and higher porosity. Furthermore, the pores were distributed more evenly at higher excipient percentages, which would be the reason for higher hardness.

With increasing the APAP content, the water penetration duration became longer. Powders with a lower contact angle penetrated faster. Particle size is a major parameter controlling granulation processes. The Tunnelling mechanism with a long penetration length was observed in 90LF-10A with fine particle size. However, in the case of coarse particles, the spreading process occurred, with a shorter penetration length. The crater mechanism was observed in the majority of the 50 percent of excipients (with longer penetration time). Other formulations had hybrid and transitional mechanisms dependent on the penetration characteristics.

The granule generated via tunneling had the lowest porosity and mean pore volume, while the granule formed by spreading had the highest porosity and mean pore volume. The porosity and mean pore volume of the granules increased as the particle size of the powder increased.

For the first time, our study employed Synchrotron X-ray imaging to observe the dynamic wet granulation process in pharmaceutical powders in real-time. During the nucleation and growth phases, an advanced understanding of pore evolution was obtained. The new findings of this study provide helpful guidelines for improving granulation operations and powder selection for the pharmaceutical sector.

5.2 Recommendations

The results of this study indicate that synchrotron X-ray computed tomography is a promising technique for studying the wet granulation process using the single drop impact method.

Further improvements can be made such as having a larger Field of View (FOV) while maintaining a high scan time.

The effect of different operating parameters, namely droplet volume, droplet release height, and temperature can be investigated.

Binary mixtures with acetaminophen were studied, however, the real formulations containing different powders used in the industry are to be explored further.

Also, the distribution of different components in final granules can be investigated; for this purpose, it is more efficient to use the components with very different densities and X-ray absorption coefficients, resulting in better contrast and less challenging image processing.

Finally, the (real-time) dynamic drying of the granules through this advanced imaging technique can be a research topic interesting to various industries where drying is a critical unit operation.

Appendix A. Sample codes for image processing and calculations

The following sample code is written in Python language.

```
import os
import subprocess
import numpy as np
from shutil import copyfile
from datetime import datetime
run = 1
starttime = datetime.now()
present_dir = os.getcwd()
def root_path():
        return os.path.abspath(os.sep)
```

################### INPUTS ###################

```
# relavant paths
PATH = "/path/to/directory/with/flats/darks/and/tomo"
SAVE = "/path/to/directory/where/to/save/reconstructed/images"
TEMP = "/path/to/directory/where/to/save/temporary/files"
if os.path.isdir(TEMP):
        # Remove temporary folder
        os.system("rm -rf "+TEMP)

# projection values
number = 500
height = 802
width = 2000
CoR = 991

# phase retreival
energy = 20
distance = 0.5
pixelsize = 5.5e-6
deltabeta = 300
regrate = 0.4339*np.log(deltabeta)+0.0034

# reconstruction y-position
y_start = 405
y_thick = 1
y_all = np.arange(np.ceil(-height/2),np.ceil(height/2+1),1)
y_some = np.arange(np.ceil(-y_thick/2),np.ceil(y_thick/2+1),1)
regionstart = y_all[y_start]
regionend = y_all[y_start+y_thick]
```

```python
# dynmaic ct subgrouping
t_start = 4000
t_last = 20000
t_step = 100


################### COMMANDS ##################

if run == 1:

        # STEP 1 - create directory variables and check darks flats and tomo
        flatsdir = os.path.join(PATH,"flats")
        darksdir = os.path.join(PATH,"darks")
        tomodir = os.path.join(PATH,"tomo")
        check1 = os.path.isdir(flatsdir)
        check2 = os.path.isdir(darksdir)
        check3 = os.path.isdir(tomodir)
        if [check1,check2,check3] == [True,True,True]:
                pass
        else:
                print("Incomplete Data")
                quit()

        # STEP 2 - make subfolder
        for j in range(t_start,t_last+t_step,t_step):
                # total number of projections in tomo
                tomonames = sorted(os.listdir(os.path.join(PATH,"tomo")))
                tomolimit = np.size(tomonames)-number+1
                if j < tomolimit:
                        print('dataset '+str(j))
                        if run == 1:
                                os.mkdir(os.path.join(TEMP))
                                os.mkdir(os.path.join(TEMP,"tomosub"))
                                for k in range(number):
                                        copyfile(os.path.join(PATH,"tomo",tomonames[k+j]),
os.path.join(TEMP,"tomosub",tomonames[k+j]))
                                # reset tomo directory variable
                        tomodir = os.path.join(TEMP,"tomosub")

                        # STEP 3 - Projection processing and CT reconstruction
                        if run == 1:
                                # tofu commands
                                # flat field correction and phase retrieval and save as proj-step1
                                os.system("tofu   preprocess   --fix-nan-and-inf   --projection-filter
none --delta 1e-6 --energy "+str(energy)+" --propagation-distance "+str(distance)+" --pixel-size
"+str(pixelsize)+" --regularization-rate "+str(regrate)+" --darks "+darksdir+" --flats "+flatsdir+" -
-projections "+tomodir+" --output "+os.path.join(TEMP,"proj-step1/proj-%04i.tif"))
```
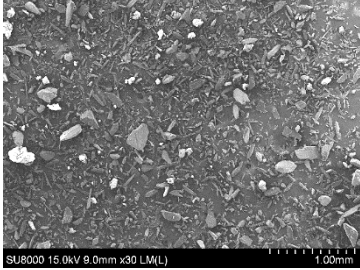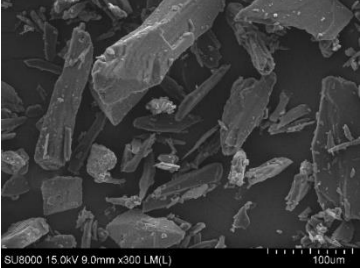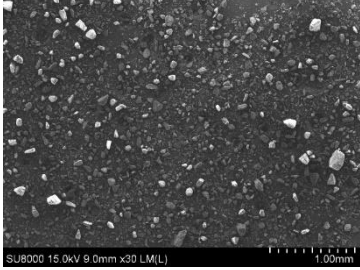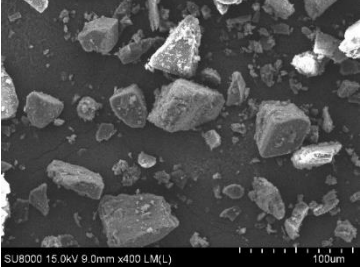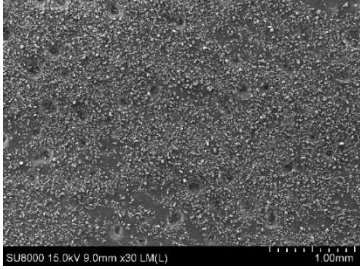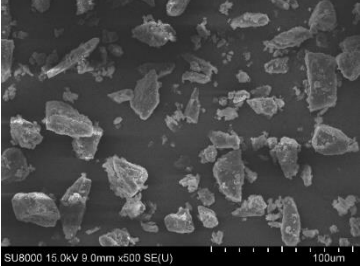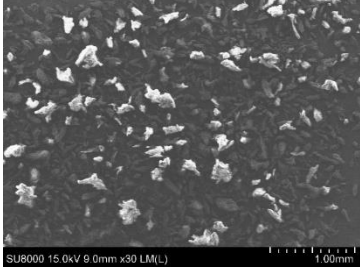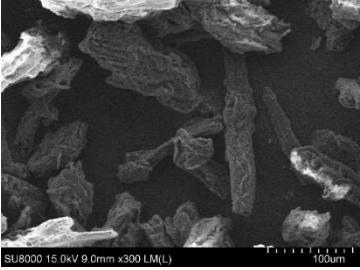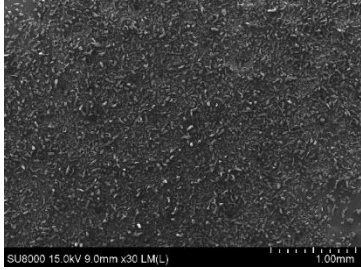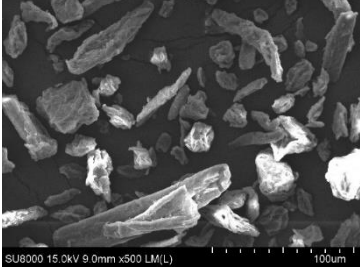
```python
                    # make proj-step1 into sinograms
                    os.system("tofu sinos --projections "+os.path.join(TEMP,"proj-
step1")+" --output "+os.path.join(TEMP,"sinos/sin-%04i.tif")+" --number "+str(number)+" --
height "+str(height)+" --output-bytes-per-file 0")
                    # apply sarepy ring removal filter to sinograms
                    os.system("python/opt/ufoenv/lib/python3.9/site-ackages/ufo_tofu-
0.13.0.dev0-py3.9.egg/tofu/ez/RR_external.py --sinos "+os.path.join(TEMP,"sinos")+" --mws 75
--mws2 91 --snr 3 --sort_only 1")
                    # make filtered sinograms back into projections and save as proj-
step2
                    os.system("tofu sinos --projections "+os.path.join(TEMP,"sinos-
filt")+" --output "+os.path.join(TEMP,"proj-step2/proj-%04i.tif")+" --number "+str(y_thick))
                    # CT reconstruction on proj-step2
                    os.system("tofu reco --overall-angle 180 --projections
"+os.path.join(TEMP,"proj-step2")+" --output "+os.path.join(SAVE,str(j).zfill(5),"sli")+" --
center-position-x "+str(CoR)+" --number "+str(number)+" --volume-angle-z 0.00000 --region=-
15,-14,1 --output-bytes-per-file 0 --slice-memory-coeff=0.7")
                    # Remove temporary folder
                    os.system("rm -rf "+TEMP)

elapsedtime = str(datetime.now()-starttime)
print ("Finisehd in "+elapsedtime)
```

Appendix B. SEM images in different magnitudes.

Magnitude / Powder	1 mm	100 um
APAP		
LMH		
LMHF		
MCC		
MCCF		

Appendix C. Permissions

In the following pages the permissions for using the figures in Chapter 2 are provided.

JOHN WILEY AND SONS LICENSE
TERMS AND CONDITIONS

Jul 28, 2022

This Agreement between Ms. Sima Zeinali Danalou ("You") and John Wiley and Sons ("John Wiley and Sons") consists of your license details and the terms and conditions provided by John Wiley and Sons and Copyright Clearance Center.

License Number	5357811488131
License date	Jul 28, 2022
Licensed Content Publisher	John Wiley and Sons
Licensed Content Publication	AIChE Journal
Licensed Content Title	A regime map for granule formation by drop impact on powder beds
Licensed Content Author	James D. Litster, Defne Kayrak-Talay, Heather N. Emady
Licensed Content Date	Nov 15, 2012
Licensed Content Volume	59
Licensed Content Issue	1

Licensed Content Pages	12

Type of use	Dissertation/Thesis

Requestor type	University/Academic

Format	Electronic

Portion	Figure/table

Number of figures/tables	1

Will you be translating?	No

Title	3D and 4D Microstructure Study of Wet Granulation Dynamics in Pharmaceutical Powders using Synchrotron X-ray Micro Computed Tomography

Institution name	University of Saskatchewan

Expected presentation date	Aug 2022

Portions	Figure 1 on page 97

Publisher Tax ID	EU826007151

ELSEVIER LICENSE
TERMS AND CONDITIONS

Jul 28, 2022

This Agreement between Ms. Sima Zeinali Danalou ("You") and Elsevier ("Elsevier") consists of your license details and the terms and conditions provided by Elsevier and Copyright Clearance Center.

License Number	5357850330689
License date	Jul 28, 2022
Licensed Content Publisher	Elsevier
Licensed Content Publication	International Journal of Pharmaceutics
Licensed Content Title	Visualization and quantitative profiling of mixing and segregation of granules using synchrotron radiation X-ray microtomography and three dimensional reconstruction
Licensed Content Author	Ruihao Liu,Xianzhen Yin,Haiyan Li,Qun Shao,Peter York,You He,Tiqiao Xiao,Jiwen Zhang
Licensed Content Date	Mar 10, 2013
Licensed Content Volume	445
Licensed Content Issue	1-2
Licensed Content Pages	9
Start Page	125

| End Page | 133 |

| Type of Use | reuse in a thesis/dissertation |

| Portion | figures/tables/illustrations |

| Number of figures/tables/illustrations | 1 |

| Format | electronic |

| Are you the author of this Elsevier article? | No |

| Will you be translating? | No |

| Title | 3D and 4D Microstructure Study of Wet Granulation Dynamics in Pharmaceutical Powders using Synchrotron X-ray Micro Computed Tomography |

| Institution name | University of Saskatchewan |

| Expected presentation date | Aug 2022 |

| Portions | Fig.6 on page 130 |

| Publisher Tax ID | GB 494 6272 12 |

| Total | 0.00 USD |

Terms and Conditions

ELSEVIER LICENSE
TERMS AND CONDITIONS

Jul 28, 2022

This Agreement between Ms. Sima Zeinali Danalou ("You") and Elsevier
("Elsevier") consists of your license details and the terms and conditions provided by
Elsevier and Copyright Clearance Center.

License Number	5357860894237
License date	Jul 28, 2022
Licensed Content Publisher	Elsevier
Licensed Content Publication	International Journal of Pharmaceutics
Licensed Content Title	Synchrotron-based X-ray in-situ imaging techniques for advancing the understanding of pharmaceutical granulation
Licensed Content Author	Chen Li,Ning Zhu,Heather N. Emady,Lifeng Zhang
Licensed Content Date	Dec 15, 2019
Licensed Content Volume	572
Licensed Content Issue	n/a
Licensed Content Pages	1
Start Page	118797
End Page	0

Type of Use	reuse in a thesis/dissertation
Portion	figures/tables/illustrations
Number of figures/tables/illustrations	1
Format	electronic
Are you the author of this Elsevier article?	No
Will you be translating?	No
Title	3D and 4D Microstructure Study of Wet Granulation Dynamics in Pharmaceutical Powders using Synchrotron X-ray Micro Computed Tomography
Institution name	University of Saskatchewan
Expected presentation date	Aug 2022
Portions	Fig. 13 on page 9.
Publisher Tax ID	GB 494 6272 12
Total	0.00 USD

Terms and Conditions

INTRODUCTION

ELSEVIER LICENSE
TERMS AND CONDITIONS

Jul 28, 2022

This Agreement between Ms. Sima Zeinali Danalou ("You") and Elsevier ("Elsevier") consists of your license details and the terms and conditions provided by Elsevier and Copyright Clearance Center.

License Number	5357861004092
License date	Jul 28, 2022
Licensed Content Publisher	Elsevier
Licensed Content Publication	International Journal of Pharmaceutics
Licensed Content Title	Study of drug particle distributions within mini-tablets using synchrotron X-ray microtomography and superpixel image clustering
Licensed Content Author	Leonie Wagner-Hattler,Gabriela Québatte,Jennifer Keiser,Joachim Schoelkopf,Christian M. Schlepütz,Jörg Huwyler,Maxim Puchkov
Licensed Content Date	Jan 5, 2020
Licensed Content Volume	573
Licensed Content Issue	n/a
Licensed Content Pages	1
Start Page	118827

End Page	0
Type of Use	reuse in a thesis/dissertation
Portion	figures/tables/illustrations
Number of figures/tables/illustrations	1
Format	electronic
Are you the author of this Elsevier article?	No
Will you be translating?	No
Title	3D and 4D Microstructure Study of Wet Granulation Dynamics in Pharmaceutical Powders using Synchrotron X-ray Micro Computed Tomography
Institution name	University of Saskatchewan
Expected presentation date	Aug 2022
Portions	Fig.2 on page 5.
Publisher Tax ID	GB 494 6272 12
Total	0.00 USD

Terms and Conditions

ELSEVIER LICENSE
TERMS AND CONDITIONS

Jul 28, 2022

This Agreement between Ms. Sima Zeinali Danalou ("You") and Elsevier
("Elsevier") consists of your license details and the terms and conditions provided by
Elsevier and Copyright Clearance Center.

License Number	5357800096841
License date	Jul 28, 2022
Licensed Content Publisher	Elsevier
Licensed Content Publication	Powder Technology
Licensed Content Title	Nucleation, growth and breakage phenomena in agitated wet granulation processes: a review
Licensed Content Author	Simon M. Iveson,James D. Litster,Karen Hapgood,Bryan J. Ennis
Licensed Content Date	Jun 4, 2001
Licensed Content Volume	117
Licensed Content Issue	1-2
Licensed Content Pages	37
Start Page	3
End Page	39

Type of Use	reuse in a thesis/dissertation
Portion	figures/tables/illustrations
Number of figures/tables/illustrations	1
Format	electronic
Are you the author of this Elsevier article?	No
Will you be translating?	No
Title	3D and 4D Microstructure Study of Wet Granulation Dynamics in Pharmaceutical Powders using Synchrotron X-ray Micro Computed Tomography
Institution name	University of Saskatchewan
Expected presentation date	Aug 2022
Portions	Fig.1 b on page 5.
Publisher Tax ID	GB 494 6272 12
Total	0.00 CAD

Terms and Conditions

INTRODUCTION

ELSEVIER LICENSE
TERMS AND CONDITIONS

Jul 28, 2022

This Agreement between Ms. Sima Zeinali Danalou ("You") and Elsevier ("Elsevier") consists of your license details and the terms and conditions provided by Elsevier and Copyright Clearance Center.

License Number	5357810538853
License date	Jul 28, 2022
Licensed Content Publisher	Elsevier
Licensed Content Publication	Chemical Engineering Journal
Licensed Content Title	A comprehensive review on process and engineering aspects of pharmaceutical wet granulation
Licensed Content Author	P. Suresh,I. Sreedhar,R. Vaidhiswaran,A. Venugopal
Licensed Content Date	Nov 15, 2017
Licensed Content Volume	328
Licensed Content Issue	n/a
Licensed Content Pages	31
Start Page	785
End Page	815

Type of Use	reuse in a thesis/dissertation
Portion	figures/tables/illustrations
Number of figures/tables/illustrations	1
Format	electronic
Are you the author of this Elsevier article?	No
Will you be translating?	No
Title	3D and 4D Microstructure Study of Wet Granulation Dynamics in Pharmaceutical Powders using Synchrotron X-ray Micro Computed Tomography
Institution name	University of Saskatchewan
Expected presentation date	Aug 2022
Portions	Fig 1 on page 788.
Publisher Tax ID	GB 494 6272 12
Total	0.00 USD

Terms and Conditions

INTRODUCTION